



A Search for H -Dropout Lyman Break Galaxies at $z \sim 12$ – 16

Yuichi Harikane^{1,2} , Akio K. Inoue^{3,4} , Ken Mawatari⁵ , Takuya Hashimoto⁶ , Satoshi Yamanaka^{4,7,8} ,
Yoshinobu Fudamoto^{4,5} , Hiroshi Matsuo^{5,9} , Yoichi Tamura¹⁰ , Pratika Dayal¹¹ , L. Y. Aaron Yung¹² , Anne Hutter¹¹ ,
Fabio Pacucci^{13,14} , Yuma Sugahara^{4,5} , and Anton M. Koekemoer¹⁵

¹ Institute for Cosmic Ray Research, The University of Tokyo, 5-1-5 Kashiwanoha, Kashiwa, Chiba 277-8582, Japan; hari@icrr.u-tokyo.ac.jp

² Department of Physics and Astronomy, University College London, Gower Street, London, WC1E 6BT, UK

³ Department of Physics, School of Advanced Science and Engineering, Faculty of Science and Engineering, Waseda University, 3-4-1 Okubo, Shinjuku, Tokyo 169-8555, Japan

⁴ Waseda Research Institute for Science and Engineering, Faculty of Science and Engineering, Waseda University, 3-4-1 Okubo, Shinjuku, Tokyo 169-8555, Japan

⁵ National Astronomical Observatory of Japan, 2-21-1 Osawa, Mitaka, Tokyo 181-8588, Japan

⁶ Tomonaga Center for the History of the Universe (TCHO), Faculty of Pure and Applied Science, University of Tsukuba, Ibaraki, 305-8571, Japan

⁷ General Education Department, National Institute of Technology, Toba College, 1-1, Ikegami-cho, Toba, Mie 517-8501, Japan

⁸ Research Center for Space and Cosmic Evolution, Ehime University, 2-5, Bunkyo-cho, Matsuyama, Ehime 790-8577, Japan

⁹ Department of Astronomical Science, The Graduate University for Advanced Studies (SOKENDAI), 2-21-1 Osawa, Mitaka, Tokyo 181-8588, Japan

¹⁰ Division of Particle and Astrophysical Science, Graduate School of Science, Nagoya University, Nagoya 464-8602, Japan

¹¹ Kapteyn Astronomical Institute, University of Groningen, P.O. Box 800, 9700 AV Groningen, The Netherlands

¹² Astrophysics Science Division, NASA Goddard Space Flight Center, Greenbelt, MD 20771, USA

¹³ Center for Astrophysics | Harvard & Smithsonian, Cambridge, MA 02138, USA

¹⁴ Black Hole Initiative, Harvard University, Cambridge, MA 02138, USA

¹⁵ Space Telescope Science Institute, 3700 San Martin Dr., Baltimore, MD 21218, USA

Received 2021 December 16; revised 2022 February 7; accepted 2022 February 8; published 2022 April 8

Abstract

We present two bright galaxy candidates at $z \sim 12$ – 13 identified in our H -dropout Lyman break selection with 2.3 deg^2 near-infrared deep imaging data. These galaxy candidates, selected after careful screening of foreground interlopers, have spectral energy distributions showing a sharp discontinuity around $1.7 \mu\text{m}$, a flat continuum at 2 – $5 \mu\text{m}$, and nondetections at $< 1.2 \mu\text{m}$ in the available photometric data sets, all of which are consistent with a $z > 12$ galaxy. An ALMA program targeting one of the candidates shows a tentative 4σ [O III] $88 \mu\text{m}$ line at $z = 13.27$, in agreement with its photometric redshift estimate. The number density of the $z \sim 12$ – 13 candidates is comparable to that of bright $z \sim 10$ galaxies and is consistent with a recently proposed double-power-law luminosity function rather than the Schechter function, indicating little evolution in the abundance of bright galaxies from $z \sim 4$ to 13 . Comparisons with theoretical models show that the models cannot reproduce the bright end of rest-frame ultraviolet luminosity functions at $z \sim 10$ – 13 . Combined with recent studies reporting similarly bright galaxies at $z \sim 9$ – 11 and mature stellar populations at $z \sim 6$ – 9 , our results indicate the existence of a number of star-forming galaxies at $z > 10$, which will be detected with upcoming space missions such as the James Webb Space Telescope, Nancy Grace Roman Space Telescope, and GREX-PLUS.

Unified Astronomy Thesaurus concepts: [Galaxy evolution \(594\)](#); [Galaxy formation \(595\)](#); [High-redshift galaxies \(734\)](#)

1. Introduction

Observing the first galaxy formation is one of the main goals in modern astronomy. One of the most straightforward approaches to achieve this goal is to observe forming galaxies directly in the early universe. Large telescopes currently in operation have yielded the most distant objects so far. These highest-redshift objects have posed various interesting questions for astronomy. For example, the most distant quasars at $z > 7$ raised a question about how to form black holes as massive as $\sim 10^9 M_\odot$ in the limited cosmic time (e.g., Mortlock et al. 2011; Bañados et al. 2018; Yang et al. 2020; Wang et al. 2021). Thus, searching for the most distant objects not only is the frontier of the knowledge of human beings but also has great power to reveal the formation physics of various objects in the early universe (e.g., see review by Stark 2016; Dayal & Ferrara 2018; Robertson 2021).

The current record of the highest-redshift galaxy spectroscopically confirmed is GN-z11 at $z \sim 11$ measured with detections of the Lyman break and rest-frame ultraviolet (UV) metal lines (Oesch et al. 2016; Jiang et al. 2021). A major surprise of GN-z11 is its remarkably high luminosity, $M_{\text{UV}} = -22.1$ mag. Given that it is not gravitationally lensed, GN-z11 is located in the brightest part of the rest-frame UV luminosity function. Although the narrow field of view (FOV) of Hubble Space Telescope (HST)/Wide Field Camera 3 (WFC3) in the near-infrared has limited the imaging survey areas to $< 1 \text{ deg}^2$, several studies using HST report very luminous Lyman break galaxies (LBGs) at $z \sim 9$ – 10 more frequently than the expectation from a Schechter-shape luminosity function (e.g., Morishita et al. 2018; Finkelstein et al. 2021a; see also Roberts-Borsani et al. 2021a). More statistically robust results have come from few-square-degree near-infrared imaging surveys with the Visible and Infrared Survey Telescope for Astronomy (VISTA) and UK Infrared Telescope (UKIRT) such as UltraVISTA (McCracken et al. 2012), the UKIRT InfraRed Deep Sky Surveys (UKIDSS; Lawrence et al. 2007), and the VISTA Deep Extragalactic Observation (VIDEO) survey (Jarvis et al. 2013). These surveys

Table 1
5 σ Limiting Magnitude of Imaging Data Used in This Study

Field	R.A.	Decl.	A_{Survey}	Subaru					VISTA/UKIRT			Spitzer	
				g	r	i	z	y	J	H	$K_s(K)$	[3.6]	[4.5]
UD-COSMOS	10:00:10	+02:12:41	1.5 deg ²	26.9	26.6	26.8	26.6	25.9	25.6/24.5	25.2/24.1	24.9/24.5	25.1	24.9
UD-SXDS	02:17:48	-05:05:44	0.8 deg ²	27.2	26.7	26.6	26.1	25.3	25.6	25.1	25.3	25.3	24.9

Notes. R.A. and decl. are the central coordinates of the survey field. The 5 σ limiting magnitudes are measured in 1''-5-, 2''-0-, and 3''-0-diameter apertures in *grizy*, $JHK_s(K)$, and [3.6][4.5] images, respectively, taken from Harikane et al. (2021b), release notes of UltraVISTA DR4^a (McCracken et al. 2012) and UKIDSS DR11^b (Lawrence et al. 2007), and Harikane et al. (2018). The values for the JHK_s bands in the UD-COSMOS field represent limiting magnitudes in the ultra-deep and deep stripes.

^a <http://ultravista.org/release4/>

^b <https://www.nottingham.ac.uk/astronomy/UDS/data/dr11.html>

have revealed that the UV luminosity functions at $z \sim 9-10$ are more consistent with a double-power-law function than a standard Schechter function (Stefanon et al. 2017, 2019; Bowler et al. 2020). Previous studies also report similar number density excesses beyond the Schechter function at $z \sim 4-7$ (Ono et al. 2018; Stevans et al. 2018; Adams et al. 2020; Harikane et al. 2022), implying little evolution of the number density of bright galaxies at $z \sim 4-10$ (Bowler et al. 2020; Harikane et al. 2022). Although spectroscopic observations are required to confirm these results, the studies indicate that there are a larger number of luminous galaxies at $z \sim 9-11$ than previously thought, which formed in the early universe of $z > 10$.

In addition to these observations of bright galaxies at $z \sim 9-11$, several studies independently suggest the presence of star-forming galaxies in the early universe even at $z \sim 15$. A candidate for a $z \sim 12$ galaxy is photometrically identified in very deep HST/WFC3 images obtained in the Hubble Ultra Deep Field 2012 (UDF12) campaign (Ellis et al. 2013). Balmer breaks identified in $z = 9-10$ galaxies indicate mature stellar populations whose ages are $\sim 300-500$ Myr, implying early star formation at $z \sim 14-15$ (Hashimoto et al. 2018; Laporte et al. 2021; see also Roberts-Borsani et al. 2020). An analysis of passive galaxy candidates at $z \sim 6$ reports that their stellar population is dominated by old stars with ages of $\gtrsim 700$ Myr, consistent with star formation activity at $z > 14$ (Mawatari et al. 2020a).

Motivated by these recent works, we search for H -band dropout (H -dropout) LBGs whose plausible redshifts are $z \sim 12-16$.¹⁶ Given the observed number density of luminous galaxies at $z \sim 9-10$ and its little redshift evolution from $z \sim 4$ to 10, it is possible that one to several $z \sim 12-16$ galaxies will be found in currently available data sets obtained by surveys with large ground- and space-based telescopes. This search for $z \sim 12-16$ galaxies is important not only for understanding early galaxy formation but also for designing survey strategies with upcoming space missions that will study the $z > 10$ universe such as the James Webb Space Telescope (JWST).

This paper is organized as follows. We describe photometric data sets and a selection of $z \sim 12-16$ galaxies in Section 2 and ALMA follow-up observations for one of our candidates in Section 3. Results of spectral energy distribution (SED) fitting and the UV luminosity function are presented in Sections 4 and 5, respectively. We discuss future prospects with space missions based on our results in Section 6, and we summarize our findings in Section 7. Throughout this paper, we use the Planck cosmological

parameter sets of the TT, TE, and EE+lowP+lensing+ext results (Planck Collaboration et al. 2016): $\Omega_m = 0.3089$, $\Omega_\Lambda = 0.6911$, $\Omega_b = 0.049$, $h = 0.6774$, and $\sigma_8 = 0.8159$. All magnitudes are in the AB system (Oke & Gunn 1983).

2. Photometric Data Set and Sample Selection

2.1. Data Set

We use deep and wide photometric data sets available in the COSMOS (Scoville et al. 2007) and SXDS (Furusawa et al. 2008) fields. The total survey area is about 2.3 deg², which is almost limited by the coverage of the deep near-infrared data. Specifically, we use optical *grizy* images obtained in the Hyper-Suprime-Cam Subaru Strategic Program (HSC-SSP) survey (Aihara et al. 2018, 2019) public data release 2 (PDR2); near-infrared JHK_s/K images of the UltraVISTA DR4 (McCracken et al. 2012) and UKIDSS UDS DR11 (Lawrence et al. 2007) in the COSMOS and SXDS fields, respectively; and Spitzer/IRAC [3.6] and [4.5] images obtained in the Spitzer Large Area Survey with Hyper-Suprime-Cam (SPLASH). Typical 5 σ limiting magnitudes of these imaging data are presented in Table 1. Since the COSMOS field has the ultra-deep and deep stripes with different depths in the near-infrared images, we use the limiting magnitude of each stripe depending on the location of the source of interest.

2.2. Selection of H -Dropout Galaxies

We construct multiband photometric catalogs in the COSMOS and SXDS fields. We start from $K_s(K)$ -band detection catalogs made by the UltraVISTA (UKIDSS) team using SExtractor (Bertin & Arnouts 1996). We select sources detected in the $K_s(K)$ bands at $>5\sigma$ levels and not detected in the J band at $>2\sigma$ levels in a 2''-diameter circular aperture. Then, we measure magnitudes of these sources in the *grizy*/ $JHK_s(K)$ images using a 2''-diameter circular aperture centered at their coordinates in the catalogs. Since point-spread functions (PSFs) of the Spitzer/IRAC [3.6] and [4.5] images are relatively large ($\sim 1''7$), source confusion and blending are significant for some sources. To remove the effects of the neighbor sources on the photometry, we first generate residual IRAC images where only the sources under analysis are left by using T-PHOT (Merlin et al. 2016), in the same manner as Harikane et al. (2018, 2019). As high-resolution prior images in the T-PHOT run, we use HSC *grizy* stacked images whose PSF is $\sim 0''7$. Then, we measure magnitudes in the IRAC images by using a 3''-diameter apertures in the same manner as Harikane et al. (2018). To account for the flux falling outside the

¹⁶ H -dropout sources searched in this work are different from previously studied dusty “ H -dropouts” at $z \sim 3-6$ (e.g., Wang et al. 2019).

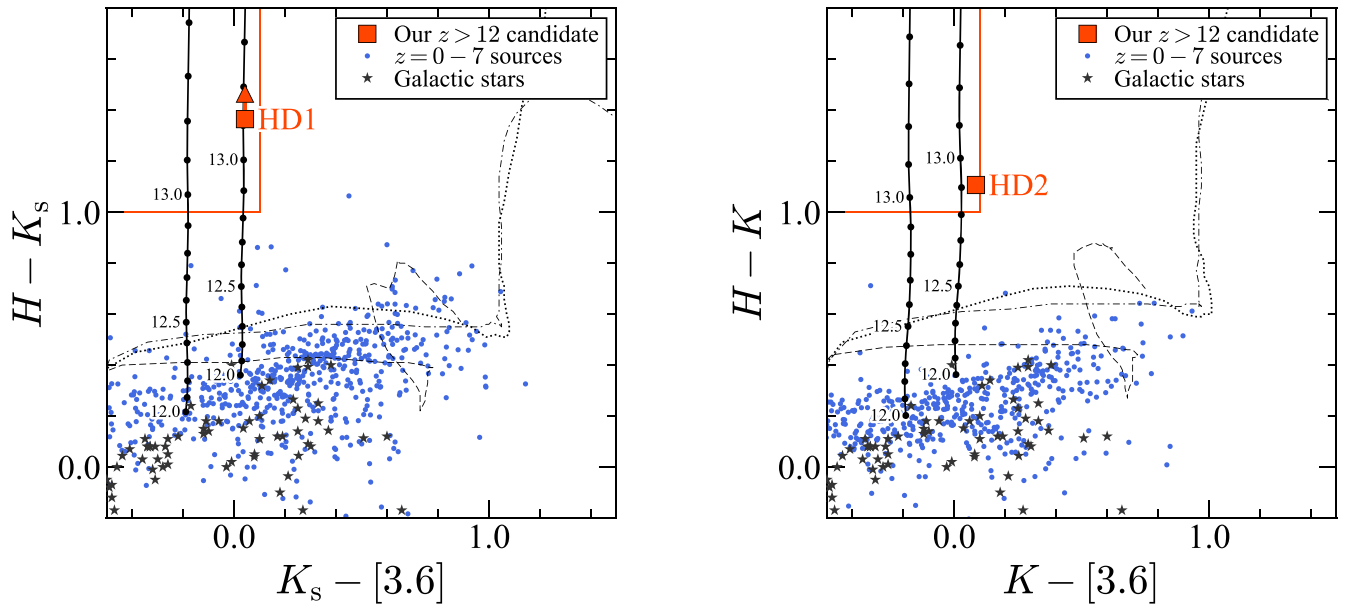


Figure 1. Two-color diagrams to select H -dropout galaxies. The left and right panels show two-color diagrams in the COSMOS and SXDS fields, respectively. The red lines indicate color criteria that we use to select H -dropout galaxies (Equations (1)–(4)), and the red squares are the selected candidates, HD1 and HD2. The black solid lines are colors of star-forming galaxies at $z \geq 12$ calculated with BEAGLE (Chevallard & Charlot 2016) with $\tau_V = 0.0$ and 0.4 (corresponding to UV spectral slopes of $\beta_{UV} \simeq -2.4$ and -1.9 , respectively) as a function of redshift. The circles on the line show their redshifts with an interval of $\Delta z = 0.1$. The blue circles are $z = 0-7$ sources spectroscopically identified (Laigle et al. 2016; Mehta et al. 2018). The dotted, dashed, and dotted-dashed lines are, respectively, typical spectra of elliptical, Sbc, and irregular galaxies (Coleman et al. 1980) redshifted from $z = 0$ to $z = 7$. The black stars indicate Galactic dwarf stars taken from Patten et al. (2006) and Kirkpatrick et al. (2011).

aperture, we apply aperture corrections derived from samples of isolated point sources in Harikane et al. (2018).

To search for $z \sim 12-16$ galaxies whose Lyman breaks are redshifted to $\sim 1.6-2.1 \mu\text{m}$, we select H -dropout LBGs from the multiband photometric catalogs constructed above. We adopt the following color selection criteria in the COSMOS and SXDS fields, respectively:

$$H - K_s > 1.0, \quad (1)$$

$$K_s - [3.6] < 0.1, \quad (2)$$

and

$$H - K > 1.0, \quad (3)$$

$$K - [3.6] < 0.1. \quad (4)$$

As shown in Figure 1, these color criteria can select sources at $z > 12$ while avoiding color tracks of $z = 0-7$ galaxies and stellar sources. To remove foreground interlopers, we exclude sources with detections at $> 2\sigma$ levels in the *grizyJ* band images. Note that we use the same values for the color criteria in the COSMOS and SXDS fields. Since the filter response profiles are different in the VISTA JHK_s filters for the COSMOS field and the UKIRT JHK filters for the SXDS field, the selection functions will not be identical. We will account for this difference by separately evaluating the selection functions in the COSMOS and SXDS fields in Section 5.1.

To remove foreground interlopers further, we conduct a photometric redshift analysis using BEAGLE (Chevallard & Charlot 2016). We adopt a constant star formation history (SFH) with the Chabrier (2003) initial mass function (IMF); stellar ages of 10^6 , 10^7 , and 10^8 yr; metallicities of 0.2 and $1 Z_\odot$; and the Calzetti et al. (2000) dust attenuation law with the V -band optical depth of $\tau_V = 0-2$ (steps of 0.2) to account for very dusty

low-redshift interlopers. We select objects whose high-redshift solution is more likely than the low-redshift ones at a $> 2\sigma$ level, corresponding to $\Delta\chi^2 > 4.0$, in the same manner as Bowler et al. (2020). Then, we visually inspect images and SEDs of the selected sources to remove spurious sources, sources affected by bad residual features in the T-PHOT-made IRAC images, and extremely red sources (e.g., $K_s(K) - [4.5] \gtrsim 1$) that are not likely to be $z \sim 12-16$ galaxies.

After these careful screening processes, we finally identify two $z \sim 12-16$ galaxy candidates, HD1 and HD2, in the COSMOS and SXDS fields, respectively. Figures 2 and 3 show images and SEDs of HD1 and HD2, and Table 2 summarizes their measured fluxes. HD1 and HD2 are spatially isolated from other nearby sources, ensuring the robustness of the photometry.

HD1 is also found in the COSMOS2020 catalog (Weaver et al. 2022). However, the photometric redshift of HD1 is 3.6 in the COSMOS2020 catalog. This is due to the difference in the measured magnitudes in the IRAC images. Our measured magnitudes are 24.6 and 24.7 mag in the [3.6] and [4.5] images, respectively, while 24.2 and 23.9 mag (24.4 and 24.1 mag) are cataloged in the COSMOS2020 CLASSIC (FARMER) catalog with very small flux errors of 3–12 nJy. If we remeasure magnitudes by using a larger aperture in the original IRAC images before the T-PHOT run, the magnitudes become brighter owing to a neighboring source located $\sim 3''/5$ from HD1. We additionally test with deeper SMUVS images (Ashby et al. 2018). We carefully measure the magnitudes in the SMUVS images and still find that the best photometric redshift for HD1 is $z > 12$. Magnitudes in the other bands, including the K_s band, in the COSMOS2020 catalog are consistent with our measurements, although their flux errors are much smaller than ours. Thus, in this study we adopt our measured magnitudes for HD1.

HD1 and HD2 will be observed in a JWST program (GO-1740; Harikane et al. 2021). In addition to these two candidates, the

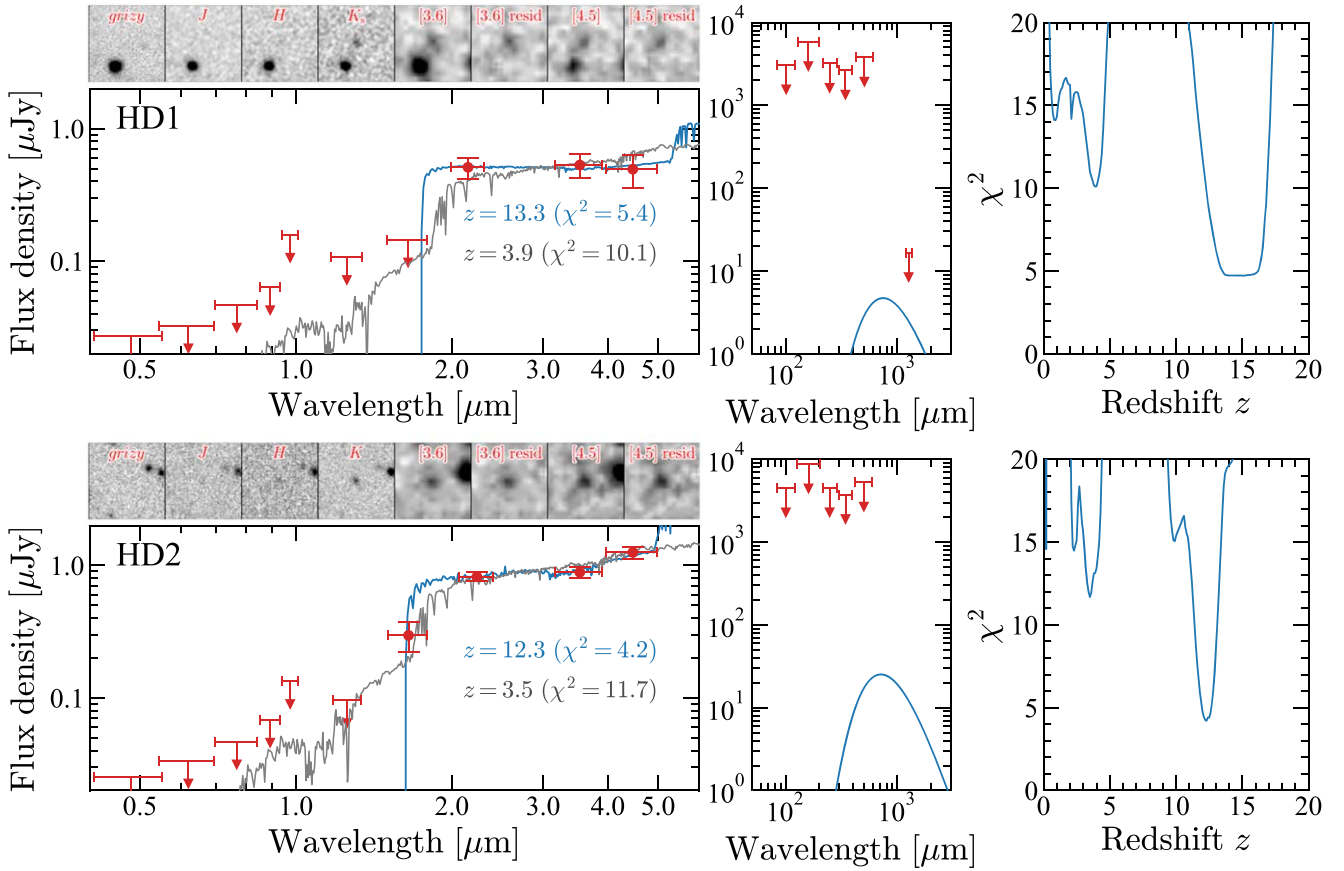


Figure 2. Left: optical to near-infrared SEDs of our H -dropout galaxy candidates, HD1 (top) and HD2 (bottom). The red symbols with error bars are measured flux densities or the 2σ upper limits. The blue curve shows the best-fit model of an LBG at $z > 12$ in the SED fitting, and the gray curve shows a passive galaxy solution at $z \sim 4$ (see Section 4). The top panels show $10'' \times 10''$ images. The “[3.6] resid” and “[4.5] resid” are residual images after subtracting nearby objects with T-PHOT (Merlin et al. 2016). Middle: the same as the left panels, but for the far-infrared to submillimeter range. The curve shows the modified blackbody function with the temperature of 50 K and the emissivity index of $\beta_{\text{dust}} = 2.0$. Right: χ^2 value as a function of the redshift. The best-fit models are found at $z > 12$.

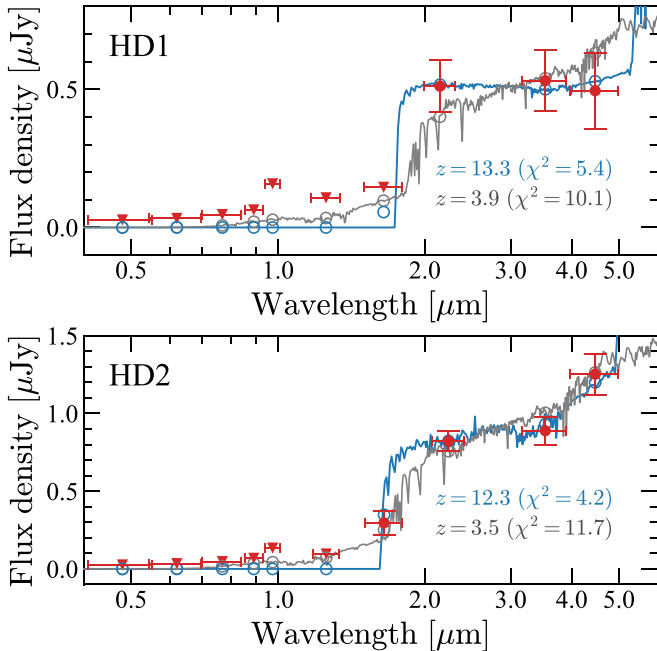


Figure 3. Same as the left panels of Figure 2, but with fluxes plotted in linear scale to compare the observed fluxes with the models. The blue and gray open circles are fluxes of the models in each band.

program will target another source, HD3 (R.A. = 02:16:54.48, decl. = -05:09:37.1), which is also a good candidate for a $z \sim 12$ –16 galaxy with its prominent break with $H - K > 1.2$ and the best photometric redshift of $z_{\text{phot}} = 14.6$. However, due to its relatively red color with $K - [3.6] = 0.2 \pm 0.2$, HD3 is not included in our final sample in this paper.

3. ALMA Follow-up Observation

We observed one of the candidates, HD1, in an ALMA Director’s Discretionary Time (DDT) program (2019.A.00015.S; PI: A. K. Inoue). Following successful detections of O III 88 μm emission lines in high-redshift galaxies (e.g., Inoue et al. 2016; Carniani et al. 2017; Laporte et al. 2017, 2021; Marrone et al. 2018; Hashimoto et al. 2018, 2019; Walter et al. 2018; Tamura et al. 2019; Harikane et al. 2020; see also Inoue et al. 2014b), we conducted a spectral scan targeting the O III 88 μm line using four tuning setups with Band 6 covering the redshift range of $12.6 < z < 14.3$. The antenna configurations were C43-2, C43-3, C43-4, and C43-5, and the typical beam size is $\sim 0''.4$ – $0''.7$. We used four spectral windows with 1.875 GHz bandwidths in the Frequency Division Mode and the total bandwidth of 7.5 GHz in one tuning setup. The velocity resolution was set to $\sim 10 \text{ km s}^{-1}$. The data were reduced and calibrated using the Common Astronomy Software (CASA;

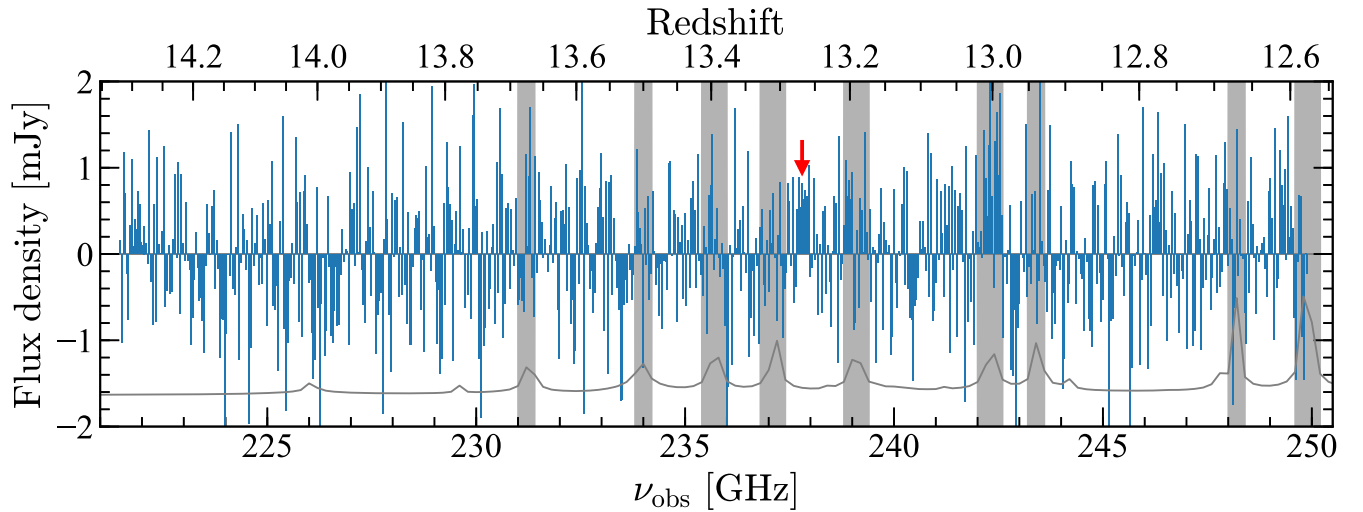


Figure 4. Full ALMA spectrum of HD1. This spectrum is extracted from a $1''$ 0-radius circular aperture centered on the coordinate of HD1. No obvious emission line is identified at $>5\sigma$, but there is a 4σ line-like feature at 237.8 GHz (red arrow), where no severe atmospheric O_3 absorption exists (gray shades).

Table 2
Photometry of Our H -Dropout Galaxy Candidates

Name	R.A.	Decl.	Subaru					VISTA/UKIRT			Spitzer	
			g	r	i	z	y	J	H	K_s/K	[3.6]	[4.5]
(1)	(2)	(3)	(4)	(5)	(6)	(7)	(8)	(9)	(10)	(11)	(12)	(13)
HD1	10:01:51.31	02:32:50.0	<27	<32	<46	<63	<157	<107	<145	510 ± 93	531 ± 108	494 ± 136
HD2	02:18:52.44	-05:08:36.1	<25	<33	<46	<68	<133	<95	296 ± 76	821 ± 63	888 ± 88	1252 ± 132

Note. Col. (1): name. Col. (2): right ascension. Col. (3): decl. Cols. (4)–(13): flux densities in nJy or 2σ upper limits.

McMullin et al. 2007) pipeline version 5.4.0 in the general manner with scripts provided by the ALMA observatory.

Figure 4 shows the obtained spectrum for HD1 extracted from a $1''$ 0-radius circular aperture. Although there is no signal at a $>5\sigma$ level, we find a 4σ tentative line-like feature around 238 GHz. As shown in the top panel of Figure 5, this feature is at 237.8 GHz, and the significance level of the peak intensity is 3.8σ in the moment 0 map shown in the bottom panel. Although there are some other line-like features (e.g., 246.3 GHz), the feature at 237.8 GHz has the highest signal-to-noise ratio among the ones in the frequencies free from severe atmospheric O_3 absorption. If this feature is the O III $88 \mu\text{m}$ emission line, the redshift of HD1 is $z = 13.27$, in good agreement with the photometric redshift estimate. A relatively broad line width ($\sim 400 \text{ km s}^{-1}$ in FWHM) is in fact comparable to similarly bright LBGs at $z \sim 6$ (Harikane et al. 2020). The emission feature is cospatial with the rest-frame UV emission in the K_s -band image (bottom panel of Figure 5). The integrated line flux is $0.24 \pm 0.06 \text{ Jy km s}^{-1}$ or $(1.9 \pm 0.5) \times 10^{-18} \text{ erg s}^{-1} \text{ cm}^{-2}$, and the line luminosity is $L_{[\text{OIII}]}$ $\simeq 3.3 \times 10^8 L_\odot$ if $z = 13.27$ is assumed.

The line luminosity is very small compared to the UV luminosity. Since the UV luminosity of HD1 is $L_{\text{UV}} = 4.8 \times 10^{11} L_\odot$, the [O III]-to-UV luminosity ratio is $L_{[\text{OIII}]} / L_{\text{UV}} \sim 7 \times 10^{-4}$. This ratio is the smallest among the galaxies observed in [O III] $88 \mu\text{m}$ emissions in the reionization epoch, as well as in the local universe so far (e.g., Inoue et al. 2016; Binggeli et al. 2021). Since the [O III]-to-UV ratio depends on the oxygen abundance (Harikane et al. 2020), this low ratio indicates a metallicity as low as ~ 0.01 – $0.1 Z_\odot$.

Another possibility is that the ALMA line scan just missed the true emission line and the redshift is out of the range of

$12.6 < z < 14.3$. As we will see in Section 5.1, the redshift selection function is as broad as $12 < z < 17$. For HD1, the lower-redshift case ($z < 12.6$) is not very favored by the SED fitting, but the higher-redshift case ($z > 14.3$) is still equally likely, as we discuss later in Section 4. Therefore, additional spectroscopic data are highly desired to confirm redshifts of HD1 and HD2. We plan to conduct follow-up observations for the tentative signal in HD1 and to newly obtain spectroscopic data for HD2 in ALMA cycle 8 (2021.1.00207.S; PI: Y. Harikane). We will also observe these candidates with JWST (GO-1740; Harikane et al. 2021), which allows us to examine a wider redshift range than ALMA.

The dust continuum of HD1 remains nondetection, which is consistent with the low-metallicity interpretation from the low $L_{[\text{OIII}]} / L_{\text{UV}}$ ratio discussed above. The obtained 1σ noise level is $8 \mu\text{Jy beam}^{-1}$. Assuming that HD1 is not resolved in this observation, we obtain a 3σ upper limit on the dust continuum of $< 24 \mu\text{Jy}$.

4. SED Fitting

To examine the photometric redshifts of HD1 and HD2 more carefully, we perform a comprehensive SED fitting analysis from optical to submillimeter wavelength using PANHIT (Mawatari et al. 2020b). PANHIT takes the energy conservation of the dust absorption in the rest-frame UV to near-infrared range and the emission in the far-infrared to submillimeter range into account. PANHIT deals with the upper limits for nondetection bands, following the probability distribution function formula proposed by Sawicki (2012). We adopt 1σ for the upper bound of the integral of the probability distribution. In addition to the fluxes in

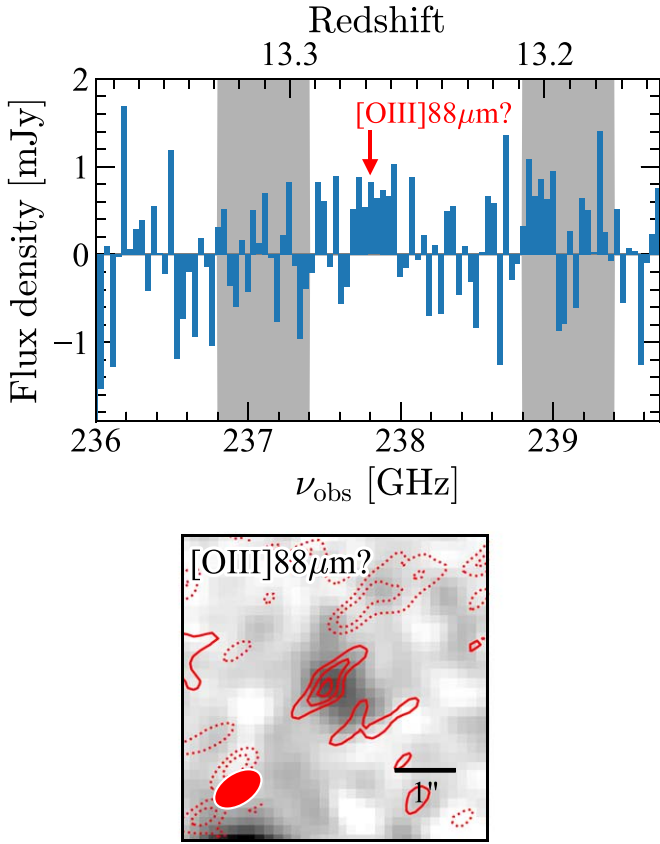


Figure 5. Top: ALMA spectrum showing the 4σ line-like feature at 237.8 GHz. This hints for the O III $88\ \mu\text{m}$ line at $z = 13.27$. Bottom: integrated intensity of the 4σ feature in HD1 overlaid on the VISTA K_s -band image. This moment 0 map is made with the CASA task `immoments`, by integrating over $700\ \text{km s}^{-1}$ covering most of the velocity range of the line emission ($>1.5\times\text{FWHM}$). The solid (dotted) lines show $+1.5\sigma$, $+2.5\sigma$, and $+3.5\sigma$ (-1.5σ , -2.5σ , and -3.5σ) contours. The emission is cospatial with the rest-frame UV emission in the K_s -band image.

grizyJHK_s(K)[3.6][4.5] measured in Section 2.2, we utilize far-infrared and submillimeter data of the Herschel survey (Oliver et al. 2012) of HD1 and HD2 and the ALMA data obtained for HD1 (see Section 3). Since dust continua of HD1 and HD2 are not detected in these data, we use the upper limits for the SED fitting.

We assume a delayed- τ model for the SFH covering a wide range of histories, including a short-timescale burst, rising, declining, and almost constant cases (Speagle et al. 2014). It is important to include passive galaxy models because the red $H-K_s(K)$ color can be produced by the Balmer break as well as the Lyman break. This may be a major contamination case in our H -dropout selection. Template spectra include the BC03 stellar population synthesis model (Bruzual & Charlot 2003) with the Chabrier (2003) IMF of $0.1\text{--}100\ M_\odot$, the nebular continuum and line emission model (Inoue 2011), and the dust thermal emission with a modified blackbody function. The dust temperature is assumed to be 30 K, 50 K, or 80 K to account for possibilities of dusty interlopers with various temperatures, and the dust emissivity index is fixed at $\beta_{\text{dust}} = 2.0$. The effect of the cosmic microwave background on the dust emission (da Cunha et al. 2013) is also taken into account.

The considered fitting parameters are as follows: the SFH timescale is $\tau_{\text{SFH}} = 0.01, 0.03, 0.06, 0.1, 0.3, 0.6, 1, 3, 6,$ and $10\ \text{Gyr}$ (10 cases); the metallicity is $Z = 0.0001, 0.0004, 0.004,$

Table 3
Physical Properties of Our H -Dropout Candidates

Name (1)	z_{phot} (2)	M_{UV} (3)	SFR_{UV} (4)	$\log M_*$ (5)	A_V (6)
HD1	$15.2^{+1.2(1.6)}_{-2.1(2.7)}^{\text{a}}$	-23.3^{a}	110^{a}	$\sim 9\text{--}11$	< 0.08
HD2	$12.3^{+0.4(0.7)}_{-0.3(0.7)}$	-23.8	170	$\sim 9.8\text{--}11$	$\lesssim 0.8$

Notes. Col. (1): name. Col. (2): the best photometric redshift with 1σ (2σ) errors. Col. (3): absolute UV magnitude in units of mag. Col. (4): SFR estimated from the UV magnitude by using Equation (7) in units of $M_\odot\ \text{yr}^{-1}$. Cols. (5) and (6): stellar mass and dust attenuation suggested by the SED fitting in units of M_\odot and mag, respectively. See Section 4 for details.

^a $z = 13.27$ is suggested by the ALMA observations for HD1 (see Section 3), consistent with the photometric redshift estimate within 1σ . The absolute UV magnitude and SFR in this table are calculated based on the assumption of $z = 13.27$.

0.008, 0.02 ($=Z_\odot$), and 0.05 (six cases); the dust attenuation is $A_V = 0.01\text{--}10$ with 20 logarithmic steps; the stellar population age is 7 cases in $1\text{--}10\ \text{Myr}$, 8 cases in $10\text{--}100\ \text{Myr}$, 15 cases in $100\ \text{Myr}\text{--}1\ \text{Gyr}$, and 8 cases in $1\text{--}15\ \text{Gyr}$, but limited by the cosmic age at the redshift of interest; and the redshift is $0.1\text{--}20.0$ with a 0.1 step assuming a flat prior.

Figure 2 shows the results of the SED fitting analyses, and Table 3 summarizes the results. The best photometric redshifts are always $z > 12$ for both HD1 and HD2 thanks to the sharp discontinuity between H and $K_s(K)$ bands. The low-redshift solutions are found at $z \sim 4$ for both objects with larger χ^2 values than the $z > 12$ solutions. These are Balmer break galaxy solutions, and the dust temperature does not affect them because these solutions have very weak or no dust emission. Another type of possible solution are dusty $H\alpha$ emitters at $z \sim 2$, although these solutions are not supported by the nondetections in the far-infrared and submillimeter bands. In these solutions, a strong $H\alpha$ line boosts $K_s(K)$ band and makes $H-K_s(K)$ color as red as $z \sim 12\text{--}16$ galaxies. In the very high dust temperature case of 80 K, this solution gives a slightly smaller χ^2 than those of the Balmer break ones at $z \sim 4$, while the lower, more normal dust temperature cases do not favor this type of solution. Moreover, even the 80 K case is significantly less likely compared to the solutions at $z > 12$ ($\Delta\chi^2 > 4$).

For HD1, the best-fit redshift is $z = 15.2$ ($\chi^2 = 4.7$), which is in fact out of the ALMA [O III] $88\ \mu\text{m}$ scan (Section 3). The case of $z = 13.3$, corresponding to the possible line feature at $z = 13.27$, gives $\chi^2 = 5.4$. Since it is roughly equally likely (within the 1σ confidence range; see Table 3), we show this case in Figure 2. The physical properties are not well constrained, except for the dust attenuation that is $A_V < 0.08$ (2σ). The stellar mass (M_*) is $(1\text{--}100) \times 10^9\ M_\odot$, depending on the stellar age that is not constrained. When the age is less than $\sim 10\ \text{Myr}$, the stellar mass and star formation rate (SFR) are estimated to be $M_* \sim 1 \times 10^9\ M_\odot$ and $\text{SFR} \sim 10^2\text{--}10^3\ M_\odot\ \text{yr}^{-1}$, respectively. For an age of $10\text{--}100\ \text{Myr}$ ($>100\ \text{Myr}$), $M_* \sim (1\text{--}10) \times 10^9\ M_\odot$ and $\text{SFR} \sim 10^2\ M_\odot\ \text{yr}^{-1}$ ($M_* \sim (10\text{--}100) \times 10^9\ M_\odot$ and $\text{SFR} < 10^2\ M_\odot\ \text{yr}^{-1}$) are obtained. The SFH timescale also produces dependencies; for $\tau_{\text{SFH}} > 100\ \text{Myr}$ (a larger value is closer to a constant SFH), we obtain $M_* \sim (1\text{--}10) \times 10^9\ M_\odot$ and $\text{SFR} \sim 10^2\text{--}10^3\ M_\odot\ \text{yr}^{-1}$, and for $\tau_{\text{SFH}} < 100\ \text{Myr}$, M_* and SFR show larger variations. The metallicity is not constrained at all.

For HD2, the best-fit redshift is $z = 12.3$ ($\chi^2 = 4.2$) and the 1σ range ($\Delta\chi^2 < 1$) is $12.0 < z < 12.7$. We find two types of high-redshift solutions. One is a very young starburst: an age

less than 10 Myr, $M_* \sim 7 \times 10^9 M_\odot$, $\text{SFR} \sim 10^3 - 10^4 M_\odot \text{ yr}^{-1}$, and $A_V \sim 0.8$. τ_{SFH} and metallicity are not constrained. The other case is a massive and relatively mature galaxy: an age greater than 100 Myr, $M_* \sim 1 \times 10^{11} M_\odot$, $\text{SFR} < 10^2 M_\odot \text{ yr}^{-1}$, $A_V < 0.5$, and $\tau_{\text{SFH}} < 60$ Myr. The metallicity is not constrained.

Although they are statistically less likely given the larger χ^2 values, the possible Balmer break solutions are as follows. For HD1, we obtain $z \sim 3.9$, age of 0.3–1 Gyr, $M_* \sim (6-10) \times 10^9 M_\odot$, $\text{SFR} < 0.1 M_\odot \text{ yr}^{-1}$, $A_V < 0.5$, $\tau_{\text{SFH}} < 0.1$ Gyr, and $Z > 0.004$. For HD2, we obtain $z \sim 3.5$, age of 0.4–0.7 Gyr, $M_* \sim 1 \times 10^{10} M_\odot$, $\text{SFR} \sim 0 M_\odot \text{ yr}^{-1}$, $A_V < 0.1$, $\tau_{\text{SFH}} < 0.03$ Gyr, and $Z > 0.02$. These stellar masses of $\sim 10^{10} M_\odot$ are ~ 10 times smaller than known passive galaxies at $z \sim 4$ (Glazebrook et al. 2017; Tanaka et al. 2019; Valentino et al. 2020). Therefore, even these cases will be interesting to examine further spectroscopically in the future.

5. Luminosity Function and SFR Density

5.1. Selection Completeness

To derive the rest-frame UV luminosity function of the $z \sim 12-16$ galaxies, we estimate the selection completeness by conducting Monte Carlo simulations. We first make mock SEDs of galaxies at $9.0 < z < 19.0$ (steps of 0.1) with UV spectral slopes of $-3.0 < \beta_{\text{UV}} < -1.0$ (steps of 0.1). The intergalactic medium attenuation is taken into account by using a prescription of Inoue et al. (2014a), resulting in almost zero flux densities at a wavelength bluer than the Ly α break. We then calculate fluxes in each band by integrating mock SEDs through our 10 filters (*grizyJHK_s(K)*[3.6][4.5]) and scale to have apparent magnitudes of 23.0–25.0 mag in the $K_s(K)$ band, whose central wavelength corresponds to ~ 1500 Å at $z \sim 13$. We then perturb the calculated fluxes by adding photometric scatters based on a Gaussian distribution with a standard deviation equal to the flux uncertainties in each band. We generate 1000 mock galaxies at each redshift with UV spectral slopes following a Gaussian distribution with a mean of $\beta_{\text{UV}} = -2.0$ and a scatter of $\Delta\beta_{\text{UV}} = 0.2$ (Rogers et al. 2014; Bowler et al. 2020). Finally, we select $z \sim 12-16$ galaxy candidates with the same color selection criteria and calculate the selection completeness as a function of the $K_s(K)$ -band magnitude and redshift, $C(m, z)$, averaged over the UV spectral slope. Figure 6 shows the calculated selection completeness in the COSMOS and SXDS fields. Our selection criteria can select sources at $12 \lesssim z \lesssim 16$. The mean redshift from the simulation is $z = 14.3$ and 14.6 in the COSMOS and SXDS fields, respectively, but in this paper we adopt $z = 12.8$ ($z \sim 13$), which is the average of the nominal redshifts for HD1 and HD2, as the mean redshift of our *H*-dropout sample. The selection completeness is $\sim 70\%$ even for very bright (23.0 mag) galaxies because our color criteria are very strict in order to remove foreground interlopers (see Figure 1) and miss some intrinsically red ($\beta_{\text{UV}} \gtrsim -1.8$) $z \gtrsim 12$ galaxies.

Based on the results of these selection completeness simulations, we estimate the survey volume per unit area as a function of the apparent magnitude (Steidel et al. 1999),

$$V_{\text{eff}}(m) = \int C(m, z) \frac{dV(z)}{dz} dz, \quad (5)$$

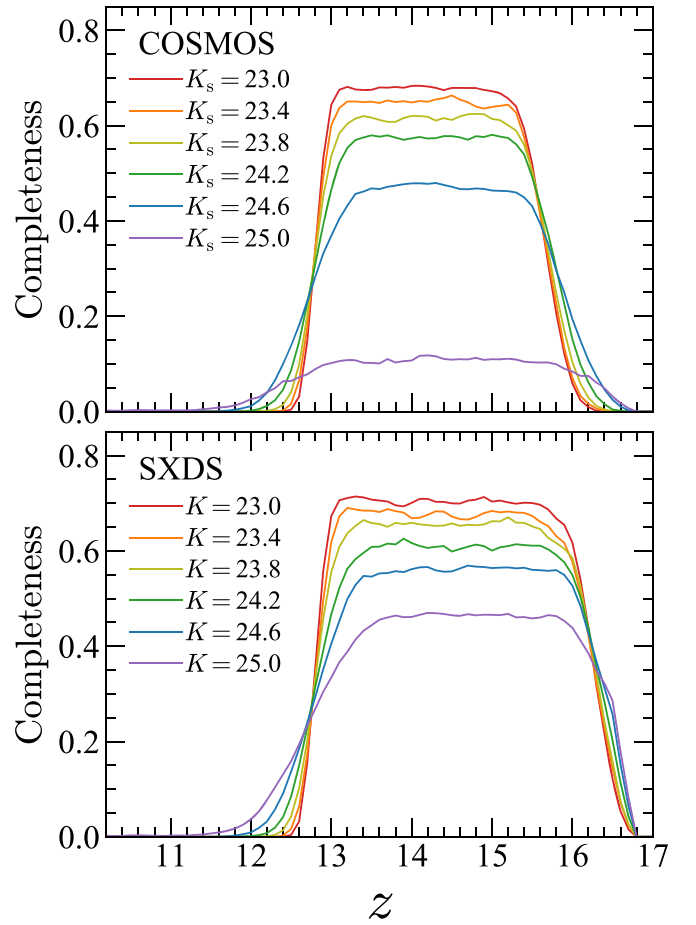


Figure 6. Completeness estimated in our Monte Carlo simulations. The top and bottom panels are results for the COSMOS and SXDS fields, respectively. The red, orange, yellow, green, blue, and purple lines show the completeness for $K_s(K) = 23.0, 23.4, 23.8, 24.2, 24.6,$ and 25.0 mag sources, respectively.

where $C(m, z)$ is the selection completeness, i.e., the probability that a galaxy with an apparent magnitude m at redshift z is detected and satisfies the selection criteria, and $dV(z)/dz$ is the differential comoving volume as a function of redshift.

5.2. Contamination

The space number density of the $z \sim 13$ galaxies that are corrected for incompleteness and contamination is calculated with the following equation:

$$\psi(m) = [1 - f_{\text{cont}}] \frac{n_{\text{raw}}(m)}{V_{\text{eff}}(m)}, \quad (6)$$

where $n_{\text{raw}}(m)$ is the surface number density of selected galaxies in an apparent magnitude bin of m , and f_{cont} is a contamination fraction. We estimate the contamination fraction of foreground sources by conducting Monte Carlo simulations. As discussed in Section 4, the most likely contaminants are $z \sim 4$ passive galaxies whose Balmer breaks mimic the Lyman break at $z \sim 13$. Stellar contaminations are not expected to be dominant, given observed colors of stellar sources (Figure 1).

To investigate contamination from various $z \sim 4$ passive galaxies, we prepare three types of mock SEDs at $3 \leq z \leq 5$ based on (1) a classic spectrum of elliptical galaxies in Coleman et al. (1980), (2) model spectra with color

distributions similar to real passive galaxies, and (3) the $z \sim 4$ solutions from the SED fittings. In case 1, we use a spectrum of old elliptical galaxies in Coleman et al. (1980) as an input SED. In case 2, we first generate model spectra of galaxies by using PANHIT assuming a delayed- τ SFH, $\tau = 0.01, 0.03, 0.1, 0.3,$ and 1 Gyr; stellar age of $0.01\text{--}1.3$ Gyr; metallicity of $Z = 0.0001, 0.0004, 0.004, 0.008, 0.02,$ and 0.05 ; and dust attenuation of $E(B-V) = 0\text{--}1$ (steps of 0.05). Then, we calculate rest-frame near-UV- r and $r\text{--}J$ colors of the models and compare these colors with those of observed passive galaxies in Davidzon et al. (2017). By selecting galaxies whose colors are consistent with the observed passive galaxies, we construct a set of passive galaxy SEDs that have realistic color distributions. In case 3, we use a spectrum of the $z \sim 4$ passive galaxy solution in the SED fitting in Section 4. Since in this case we assume that all of the passive galaxies have the same SED as the $z \sim 4$ solution, this case provides the most conservative estimate for the contamination fraction (i.e., the highest contamination fraction).

We then make mock SEDs redshifted to $3 \leq z \leq 5$ (steps of 0.1) from the three types of the SEDs, calculate fluxes in each band, scale to have stellar masses of $10^9 \leq M_*/M_\odot \leq 10^{11}$ (steps of 0.1 dex), and perturb the calculated fluxes by adding photometric scatters in the same manner as Section 5.1. We generate ~ 1000 mock galaxies at each redshift and stellar mass bin and calculate the fraction of passive galaxies that satisfy our selection criteria in each bin. Finally, by integrating the product of the stellar mass function of passive galaxies in Davidzon et al. (2017) and the fraction of passive galaxies satisfying our selection criteria over the redshift and stellar mass, we calculate the number of passive galaxies at $z \sim 4$ that are expected to be in our $z \sim 13$ galaxy sample.

The expected numbers of passive galaxies in our sample are $N_{\text{cont}} = 0.00, 0.12,$ and 1.36 in cases 1, 2, and 3, respectively. We estimate the contamination fraction f_{cont} by dividing the expected number of passive galaxies by the number of our $z \sim 13$ candidates. The estimated contamination fractions are small in cases 1 and 2 ($f_{\text{cont}} \sim 0\%$ and 6% , respectively) and $f_{\text{cont}} \sim 70\%$ in case 3, where we assume that all of the passive galaxies have the same SED as the $z \sim 4$ solution in the SED fitting as the extremely conservative case. Although the realistic simulation with the observed color distributions (i.e., case 2) indicates the very low contamination fraction, we adopt this very conservative estimate from case 3 for the UV luminosity function calculation. Note that even if we assume this conservative estimate as the prior, the $z > 12$ solutions for HD1 and HD2 in the SED fitting are still more likely than the $z \sim 4$ solutions that give larger χ^2 values, as long as the true number density of $z \sim 13$ galaxies is $\gtrsim 10^{-8} \text{ Mpc}^{-3}$ (comparable to our estimate in Section 5.3). On the other hand, if the true number density is $\sim 10^{-11} \text{ Mpc}^{-3}$ at $z \sim 13$ (comparable to model predictions in Section 5.4), the $z \sim 4$ solutions are more likely due to the higher number density of $z \sim 4$ passive galaxies compared to that of $z \sim 13$ galaxies.

5.3. UV Luminosity Function

We convert the number density of $z \sim 13$ galaxies as a function of apparent magnitude, $\psi(m)$, into the UV luminosity functions, $\Phi[M_{\text{UV}}(m)]$, which are the number densities of galaxies as a function of rest-frame UV absolute magnitude. We calculate the absolute UV magnitudes of galaxies from their apparent magnitudes in the $K_s(K)$ band, whose central

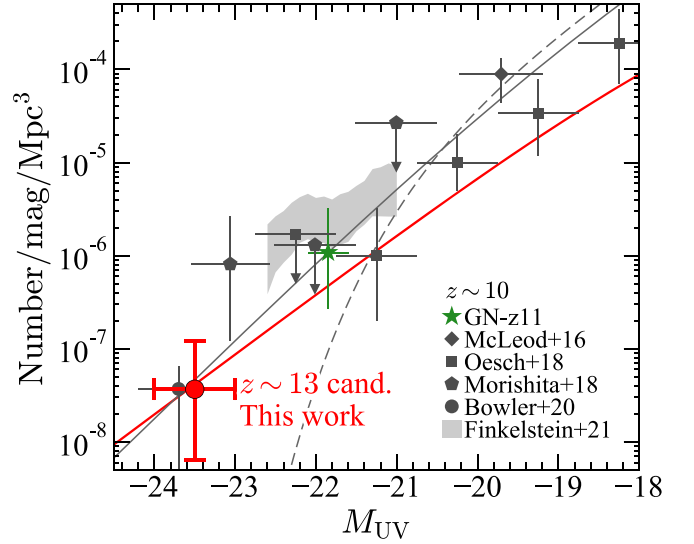


Figure 7. Rest-frame UV luminosity functions at $z \sim 13$ and $z \sim 10$. The red circle shows the number density of our $z \sim 13$ candidates. The black symbols and the gray shaded region are measurements at $z \sim 10$ from the literature (diamond: McLeod et al. 2016; square: Oesch et al. 2018; pentagon: Morishita et al. 2018; circle: Bowler et al. 2020; shade: Finkelstein et al. 2021a). The green star is the number density of GN-z11 (see text). Note that the data point of Bowler et al. (2020; GN-z11) is horizontally (vertically) offset by -0.2 mag ($+0.03$ dex) for clarity. The gray dashed line is the Schechter function fit (Bouwens et al. 2016), whereas the gray and red solid lines are the double-power-law functions at $z \sim 10$ and 13 , respectively, whose parameters are determined by the extrapolation from lower redshifts in Bowler et al. (2020).

wavelength corresponds to $\sim 1500 \text{ \AA}$ at $z \sim 13$, assuming a flat rest-frame UV continuum, i.e., constant f_ν , suggested by the SEDs of our galaxies. The 1σ uncertainty is calculated by taking into account the Poisson confidence limit (Gehrels 1986) on the expected number of galaxies at $z \sim 13$ in our sample ($N = 2 \times (1 - f_{\text{cont}}) \sim 1$).

Figure 7 shows the calculated UV luminosity function at $z \sim 13$. The number density of our $z \sim 13$ galaxies is $(3.7_{-3.0}^{+8.4}) \times 10^{-8} \text{ Mpc}^{-3} \text{ mag}^{-1}$ at $M_{\text{UV}} = -23.5$ mag. This number density is comparable to that of bright galaxies at $z \sim 10$ in Bowler et al. (2020), which is supported by the little evolution of the abundance of bright galaxies found by previous studies at $z = 4\text{--}10$ (Bowler et al. 2020; Harikane et al. 2022). Indeed, as shown in Figure 8, the number density of bright ($M_{\text{UV}} < -23$ mag) galaxies does not show significant redshift evolution from $z \sim 4$ to $z \sim 13$. In Figure 7, we also plot the number density of $z \sim 10$ galaxies estimated from GN-z11, $(1.0_{-0.8}^{+2.2}) \times 10^{-6} \text{ Mpc}^{-3}$.¹⁷ These results and the spectroscopic confirmation of GN-z11 by Oesch et al. (2016) and Jiang et al. (2021) indicate that the bright end of the luminosity function at high redshift cannot be explained by the Schechter function with the exponential cutoff and is more consistent with the double-power-law function. Indeed, the number density of our $z \sim 13$ galaxies is consistent with the double-power-law function with $M_{\text{UV}}^* = -17.6$ mag, $\phi^* = 1.0 \times 10^{-4} \text{ Mpc}^{-3}$, $\alpha = -1.8$, and $\beta = -2.6$ (Figure 7), which are derived by extrapolating the redshift evolution of the parameters in

¹⁷ This number density is lower than that in Bowler et al. (2020) because we adopt the number density estimate of Oesch et al. (2018). The UV magnitude of GN-z11 is estimated to be -22.1 and -21.6 mag in Oesch et al. (2016) and Oesch et al. (2018), respectively. We adopt their average value, -21.85 ± 0.25 mag, which is consistent with the recent estimate by Tacchella et al. (2021).

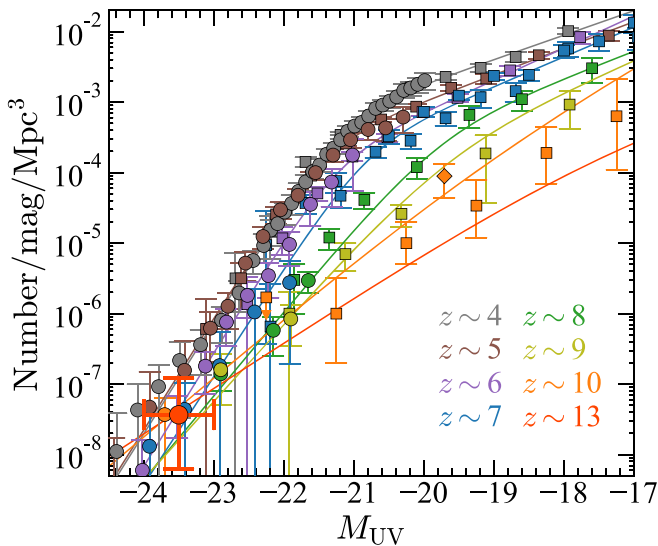


Figure 8. Evolution of the rest-frame UV luminosity functions from $z \sim 4$ to $z \sim 13$. The red circle shows the number density of our $z \sim 13$ galaxy candidates, and the gray, brown, purple, blue, green, yellow, and orange symbols show results at $z \sim 4, 5, 6, 7, 8, 9,$ and 10 , respectively. The circles at $z \sim 4-7$ are galaxy number densities from Harikane et al. (2021b), and those at $z \sim 8-10$ are taken from Bowler et al. (2020). The squares show results taken from Bouwens et al. (2021) and Oesch et al. (2018) at $z \sim 4-9$ and $z \sim 10$, respectively. The diamond is a result in McLeod et al. (2016). The lines show double-power-law functions in Harikane et al. (2021b) at $z \sim 4-7$ and Bowler et al. (2020) at $z \sim 8-13$. Note that the data point of Bowler et al. (2020) at $z \sim 10$ is horizontally offset by -0.2 mag for clarity.

Bowler et al. (2020) to $z = 13$.¹⁸ Although spectroscopic confirmation is needed, these results indicate that upcoming surveys will detect a number of galaxies at $z > 10$, which will be discussed in Section 6.

5.4. Comparison with Models

Both theoretical and empirical models predict the UV luminosity function of galaxies at $z > 10$ (e.g., Dayal et al. 2014, 2019; Mason et al. 2015; Tacchella et al. 2018; Behroozi et al. 2019, 2020; Yung et al. 2019, 2020; see also Hutter et al. 2021). We compare the number densities at $z \sim 10$ and 13 with predictions from these models in Figure 9. At $z \sim 10$, the predictions roughly agree with the observed number densities for relatively faint galaxies ($M_{UV} \gtrsim -21$ mag), but the models underestimate the number densities of bright galaxies ($M_{UV} \lesssim -22$ mag), albeit with large uncertainties in the observations. Similarly at $z \sim 13$, the models cannot reproduce the observed number density of our $z \sim 13$ galaxy candidates. These discrepancies indicate that the current models do not account for the rapid mass growth within the short physical time since the big bang.

There are several possible physical processes to reconcile these discrepancies between the models and the observations at $z \sim 10-13$. As discussed in Harikane et al. (2021b), less efficient mass quenching and/or lower dust obscuration than assumed in the models can explain the existence of these UV-bright galaxies. Active galactic nucleus (AGN) activity may also boost the UV luminosity in these galaxies. Previous

¹⁸ The extrapolated double-power-law luminosity function from Bowler et al. (2020) predicts a ~ 2 times higher number density at $z \sim 11-12$ than those at $z \sim 10$ and 13 in the magnitude regime of $M_{UV} \simeq -23.5$ mag, but still consistent with our $z \sim 13$ estimate within the errors. The details of such a redshift evolution are beyond the scope of this paper.

studies indicate that the AGN fraction starts to increase at $M_{UV} \simeq -22$ mag (Ono et al. 2018; Stevans et al. 2018; Adams et al. 2020; Harikane et al. 2022; see also Piana et al. 2022). If we assume that the UV luminosities of HD1 and HD2 are solely powered by black holes, the inferred black hole masses are $\sim 10^8 M_\odot$, assuming accretion at the Eddington rate (Pacucci et al. 2022), in accordance with expectations for high-redshift quasars (see, e.g., Haiman & Menou 2000 and Willott et al. 2010). In addition, note that a $\sim 10^8 M_\odot$ black hole at $z \sim 12$ could be the progenitor of $z \sim 7$ quasars, as the growth time to reach a mass of $10^9-10^{10} M_\odot$, typical of $z > 6$ quasars detected thus far, is shorter than the cosmic time between $z = 12-13$ and $z = 7$, for an Eddington-limited accretion. It is also possible that the observed bright sources at $z \sim 10-13$ are galaxies in a short-time starburst phase that is not captured in the models whose outputs are averaged over a time interval (see also Dayal et al. 2013). Finally, a top-heavier IMF would explain the discrepancies by producing more UV photons at the same stellar mass. It is possible that these bright galaxies (especially HD1 and HD2) are merging systems that are not resolved in the ground-based images. However, even if they are major mergers, the UV luminosity will decrease only by a factor of a few, which would not explain the discrepancy at $z \sim 13$ (see also discussions in Harikane et al. 2022; Shibuya et al. 2022). In any case, if these bright $z \sim 10-13$ galaxies are spectroscopically confirmed, the discrepancies will motivate the exploration of new physical processes that are responsible for driving the formation of these bright galaxies in the early universe.

5.5. Cosmic SFR Density

We calculate the cosmic SFR density at $z \sim 13$ by integrating the rest-frame UV luminosity function. We use a double-power-law luminosity function at $z = 13$ with $M_{UV}^* = -17.6$ mag, $\phi^* = 1.0 \times 10^{-4} \text{ Mpc}^{-3}$, $\alpha = -1.8$, and $\beta = -2.6$, which is consistent with our number density measurement (see Section 5.3). We obtain the UV luminosity density by integrating the luminosity function down to -17 mag as in previous studies (e.g., Bouwens et al. 2015, 2020; Finkelstein et al. 2015; Oesch et al. 2018). We then convert the UV luminosity density to the SFR density by using the calibration used in Madau & Dickinson (2014) with the Salpeter (1955) IMF:

$$\text{SFR}_{UV} (M_\odot \text{ yr}^{-1}) = 1.15 \times 10^{-28} L_{UV} (\text{erg s}^{-1} \text{ Hz}^{-1}). \quad (7)$$

This SFR density estimation is true only if the rest-frame UV galaxy identification is complete with respect to all the galaxy populations at $z \sim 13$ (but see Fudamoto et al. 2020). The uncertainty of the SFR density is scaled from that of the number density measurement.

The estimated SFR density is $\rho_{\text{SFR}} = (8.0_{-6.6}^{+18.4}) \times 10^{-5} M_\odot \text{ yr}^{-1} \text{ Mpc}^{-3}$ at $z = 12.8$. We compare the SFR density with previous results in Figure 10. The estimated SFR density at $z \sim 13$ is consistent with the fitting function in Harikane et al. (2021b), which is calibrated with recent observations at $z > 4$ showing a more rapid decline ($\propto 10^{-0.5(1+z)}$) than the extrapolation of the fitting function in Madau & Dickinson (2014) at $z > 10$. Furthermore, if we divide our sample into one galaxy at $z \sim 12$ and another at $z \sim 13$, given the low completeness at $z = 12.3$ (see Figure 6), the estimated SFR density would show a decrease from $z \sim 12$ to 13 , consistent

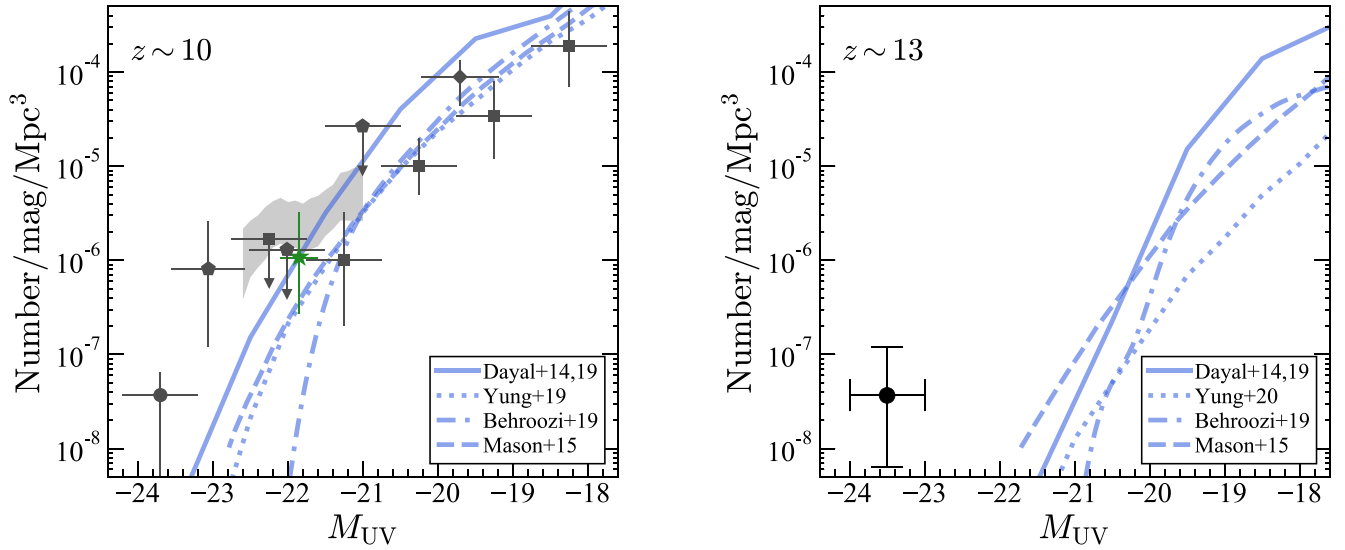


Figure 9. Comparison with predictions from theoretical and empirical models at $z \sim 10$ (left) and $z \sim 13$ (right). The black symbols and the gray shaded region are measurements at $z \sim 10$ from the literature (symbols are the same as in Figure 7) and at $z \sim 13$ from this study. The blue lines show predictions from models (solid: Dayal et al. 2014, 2019; dotted: Yung et al. 2019, 2020; dotted-dashed: Behroozi et al. 2019, 2020; dashed: Mason et al. 2015).

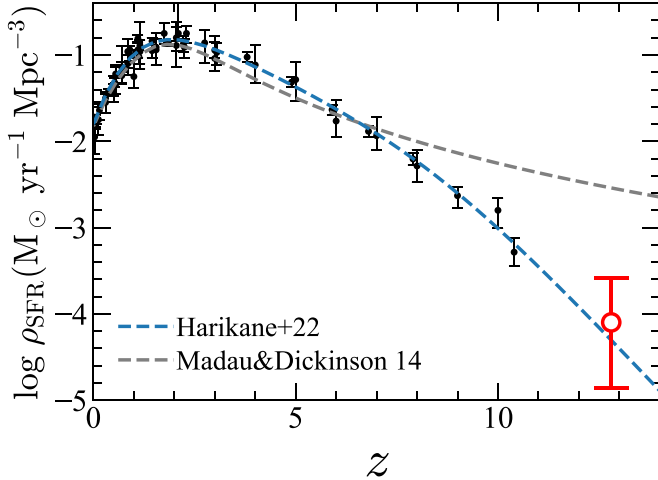


Figure 10. Evolution of the cosmic SFR density. The red circle is our result at $z \sim 13$ estimated by integrating the double-power-law luminosity function down to -17 mag. The black circles are observed cosmic SFR densities taken from Madau & Dickinson (2014), Finkelstein et al. (2015), McLeod et al. (2016), and Bouwens et al. (2020). The blue and gray dashed curves represent the fits in Harikane et al. (2021b, their Equation (60)) and Madau & Dickinson (2014, extrapolated at $z > 8$), respectively. All results are converted to use the Salpeter (1955) IMF (Equation (7)).

with Harikane et al. (2021b). The estimate is also comparable to the edge of the range of the SFR density at $z \gtrsim 13$ expected from passive galaxies at $z \sim 6$ in Mawatari et al. (2020a). Note that our estimated SFR density is dominated by relatively faint ($M_{UV} \gtrsim -20$ mag) galaxies (see Roberts-Borsani et al. 2021a for discussions at $z \sim 8-10$). In this calculation, we need to assume the shape of the UV luminosity function, because there is no constraint on the number density of faint galaxies at $z \sim 13$. Future JWST observations will measure the number density of faint $z \sim 13$ galaxies and constrain the shape of the luminosity function combined with this work for bright galaxies, allowing a more robust measurement of the SFR density.

6. Future Prospects

There are several upcoming space-based missions that can search for $z > 10$ galaxies, such as JWST, Nancy Grace Roman Space Telescope (hereafter Roman), and Galaxy Reionization EXplorer and PLANetary Universe Spectrometer (GREX-PLUS). By taking advantage of the sensitivity of infrared observations in space, these missions are expected to detect galaxies at $z > 10$. In this section, we will discuss future prospects of these space missions based on our result of the $z \sim 12-16$ galaxy search.

We here consider three missions, JWST, Roman, and GREX-PLUS, whose survey parameters are summarized in Table 4. Although Euclid has a remarkable capability to conduct wide-field surveys, it has a limited wavelength coverage to the H band and can only select sources up to $z \sim 10$ (J -dropout). We detail the three missions and survey plans below.

JWST is NASA's infrared space telescope that was launched on 2021 December 25. Thanks to its large 6.5 m diameter mirror, the sensitivity of JWST in the infrared is much higher than previous and current observational facilities. NIRCcam is a near-infrared camera at $0.6-5.0 \mu\text{m}$ whose FOV is roughly $2 \times 2.2 \times 2.2 \text{ arcmin}^2$ (Rieke et al. 2005). In this paper we consider the following six surveys using NIRCcam: the JWST Advanced Deep Extragalactic Survey (JADES; Guaranteed Time Observation (GTO) program; Eisenstein et al. 2017a, 2017b), the Cosmic Evolution Early Release Science (CEERS) survey (ERS-1345; Finkelstein et al. 2017), the COSMOS-Web survey (GO-1727; Kartaltepe et al. 2021), Public Release IMAGING for Extragalactic Research (PRIMER; GO-1837; Dunlop et al. 2021), the Next Generation Deep Extragalactic Exploratory Public (NGDEEP) survey (GO-2079; Finkelstein et al. 2021b), and the Parallel wide-Area Nircam Observations to Reveal And Measure the Invisible Cosmos (PANORAMIC) survey (GO-2514; Williams et al. 2021). These surveys will take deep NIRCcam imaging data at $\sim 1-5 \mu\text{m}$ in $\sim 10-2000 \text{ arcmin}^2$ survey fields. Other high-redshift galaxy surveys are also planned in Cycle 1. For

Table 4
Expected Number of $z \gtrsim 13$ Galaxies Identified in Upcoming Surveys

Telescope (1)	Survey (2)	$m_{5\sigma}$ (3)	A_{survey} (4)	$N(z \sim 13)$ (5)	$N(z \sim 15)$ (6)	$N(z \sim 17)$ (7)
JWST	JADES/Deep	30.6/30.2	0.013	11–0.5	1–0	0–0
	JADES/Medium	29.7/29.3	0.053	15–0.5	1–0	0–0
	CEERS	29.0/29.2	0.027	3–0	0.5–0	0–0
	COSMOS-Web	–/28.1 ^a	0.6	19–0.5	2–0	0–0
	PRIMER	$\leq 27.8 / \leq 27.7^b$	0.111	5–0	0.5–0	0–0
	NGDEEP	30.6/30.7	0.0027	2–0	1–0	0–0
Roman	PANORAMIC	28.3/28.3	0.4	17–0.5	2–0	0–0
	UltraDeep	29.6/28.6	1	250–7 ^c	5–0	...
	Deep	27.5/27.2	20	270–3 ^c	9–0	...
	HLS	26.7/-	2000	8441–33 ^c
GREX-PLUS	UltraDeep	27.7	1	18–0	1–0	0–0
	Deep	27.0	40	262–2	17–0	1–0
	Medium	26.0	200	300–0	17–0	1–0
	Wide	24.5	2000	322–0	14–0	0.5–0

Notes. Col. (1): telescope. Col. (2): planned survey. Col. (3): 5σ depth in the AB magnitude in the rest-frame UV band. In JWST, we quote depths of the F200W and F227W bands for the $z \sim 13$ and $z \sim 15$ –17 galaxy selections, respectively. In Roman, depths of the F184 and K213 bands are quoted for the $z \sim 13$ and $z \sim 15$ galaxy selections, respectively. In GREX-PLUS, we quote depths in the F232 band for the $z \sim 13$ –17 galaxy selection. These depths are for point sources for simplicity, and the actual depths for high-redshift galaxies would be slightly shallower, except in PRIMER and NGDEEP, where resolved sources with typical sizes of high-redshift galaxies are assumed. Col. (4): survey area in deg^2 . Cols. (5)–(7): expected number of galaxies at $z \sim 13$, 15, and 17 identified in the survey assuming $\Delta z = 1$. Two values indicate the numbers in case A and case B (see text for details). Note that it may be difficult to select $z \sim 17$ sources with Roman owing to the lack of observational bands redder than the K213 band. Because the current plan of the Roman HLS does not include the K213 imaging, we do not calculate the expected number of $z \sim 15$ galaxies.

^a The COSMOS-Web survey will take NIRCcam F115W, F150W, F277W, and F444W images. We use the depth of the F277W band for the $z \sim 13$ –17 galaxy selections.

^b PRIMER is a “wedding cake” survey that is composed of several surveys with different depths and areas (27.8/27.7 mag for 400 arcmin², 28.3/28.3 mag for 300 arcmin², and 28.8/28.8 mag for 33 arcmin²).

^c Although the expected number in the Roman HLS is larger than those in the other two Roman surveys, these three surveys will identify galaxies in different luminosities and are complementary to each other. Please see Figure 11 for luminosity ranges that each survey covers.

example, Through the Looking GLASS (ERS-1324; Treu et al. 2017) and the Ultra-deep NIRCcam and NIRSspec Observations Before the Epoch of Reionization (UNCOVER; GO-2561; Labbe et al. 2021) will image the gravitational lensing cluster A2744 with NIRCcam. The Webb Medium-Deep Field survey (GTO-1176; Windhorst et al. 2017) will use 110 hr to observe 13 medium-deep (28.4–29.4 mag) fields, including the JWST North Ecliptic Pole Time-domain Field (Jansen & Windhorst 2018).

Roman is NASA’s optical to near-infrared space telescope whose launch is targeted around the mid-2020s. Although the size of the mirror is comparable to that of HST, Roman is expected to conduct wide-field surveys in the near-infrared by taking advantage of the wide FOV of its camera (0.28 deg^2). The High Latitude Survey (HLS) will take images in the Y106, J129, H158, and F184 bands over the $\sim 2000 \text{ deg}^2$ sky, reaching ~ 26.7 mag in F184. Two additional survey concepts are potentially possible: the Roman ultra-deep field survey (hereafter UltraDeep; Koekemoer et al. 2019), which will take very deep images (reaching ~ 30 mag in the bluer filters and 29.6 and 28.6 mag in F184 and K213, respectively) in a small area ($\lesssim 1 \text{ deg}^2$), and the Roman cosmic dawn survey (hereafter Deep; see also Rhoads et al. 2018), which will conduct a relatively wide and deep survey ($\sim 20 \text{ deg}^2$, 27.5 and 27.2 mag in F184 and K213).¹⁹ Both of these two possible surveys would cover a wavelength range up to 2.3 μm (the K213 filter),

allowing us to select $z \sim 15$ galaxies with the F184-dropout selection.

GREX-PLUS is a new 1.2 m class, cryogenic, wide-field infrared space telescope mission concept proposed to ISAS/JAXA for its launch around the mid-2030s. GREX-PLUS is planned to have a wide-field camera that will efficiently take wide and deep images at 2–10 μm , allowing us to select galaxies at $z \sim 10$ –17. Four surveys with different depths and areas (UltraDeep, Deep, Medium, and Wide) are now being planned.

For the surveys by these three missions, we calculate the expected number of detected galaxies at $z \sim 13$, 15, and 17. For simplicity, we assume the survey volume of $\Delta z = 1$ and 100% completeness. We calculate the number of galaxies based on two cases of the rest-frame UV luminosity functions (case A and case B). One is the double-power-law function with a redshift evolution suggested in Bowler et al. (2020; case A), which is consistent with the number density of our $z \sim 13$ galaxies. The other is the Schechter function with a density evolution, whose parameters are $M_{\text{UV}}^* = -20.5$ mag, $\phi^* = 44.7 \times 10^{-0.6(1+z)} \text{ Mpc}^{-3}$, and $\alpha = -2.3$ (case B). We assume a relatively rapid decrease of the ϕ^* parameter compared to the cosmic SFR density evolution at $z > 10$ ($\propto 10^{-0.5(1+z)}$; Harikane et al. 2022), as a conservative estimate. These parameters are comparable to measurements for the $z \sim 10$ UV luminosity function in Oesch et al. (2018). These two cases mostly cover the range of model predictions at $z \sim 13$ as we show later in Figure 11. Given that these two cases are somewhat consistent with the model predictions and observations at $z \sim 10$ and 13, we extrapolate these calculations to

¹⁹ The sensitivities of the survey are calculated based on the tables on the following website: https://roman.gsfc.nasa.gov/science/anticipated_performance_tables.html.

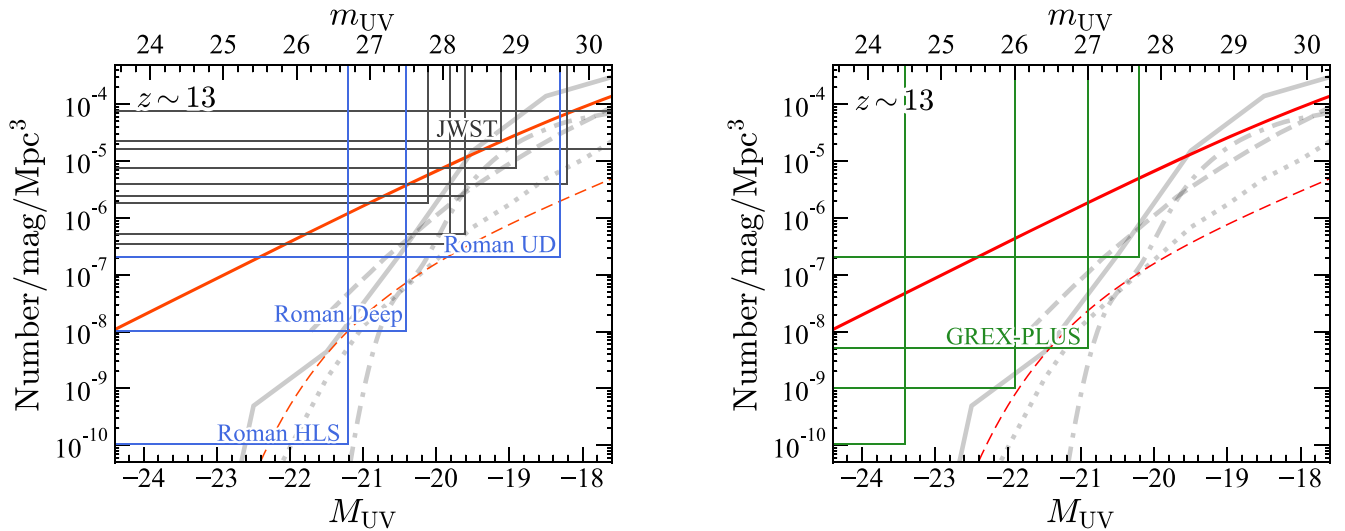


Figure 11. Predicted UV luminosity functions and the depths and volumes of upcoming surveys. The red solid and dashed lines are the double-power-law and Schechter functions (case A and case B in the text), respectively, whose parameters are determined by the extrapolation from lower redshifts (see text for details). The black, blue (left), and green (right) lines indicate expected depths and volumes of upcoming surveys with JWST, Roman, and GREX-PLUS, respectively. The gray lines show predictions from models (solid: Dayal et al. 2014, 2019; dotted: Yung et al. 2019, 2020; dotted-dashed: Behroozi et al. 2019, 2020; dashed: Mason et al. 2015, same as the right panel of Figure 9).

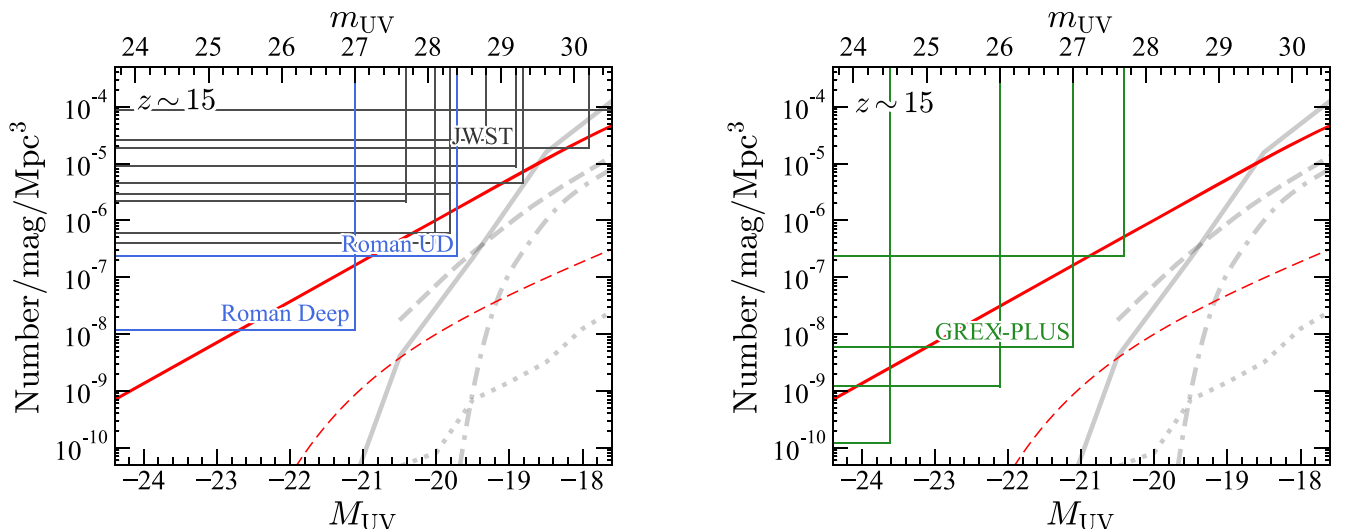


Figure 12. Same as Figure 11, but for $z \sim 15$. The 6σ depth is used for Roman to reduce the false-positive rate in the one-band (K213) detection.

$z \sim 15$ and 17 for reference. We integrate the luminosity functions down to the depths of detection bands presented in Table 4, and we calculate the number of detected galaxies at each redshift for each survey. Note that the 6σ depth is used for the $z \sim 15$ galaxies identified with Roman to reduce the false-positive rate in the one-band (K213) detection, while the 5σ depth is adopted for the others because multiple bands can be used.

Figures 11, 12, and 13 show the expected UV luminosity functions in case A and case B and the depth and volume of each survey at $z \sim 13$, 15, and 17, respectively, with predictions from models at $z \sim 13$ and 15. Table 4 summarizes the expected number of detected galaxies in each survey. JWST will identify galaxies up to $z \sim 15$ in case A. In addition, JWST can conduct deep photometric and spectroscopic observations for relatively bright $z > 10$ galaxies identified in surveys with JWST and other telescopes, which will allow us to investigate

physical properties (e.g., systemic redshift, stellar age, metallicity) in detail (e.g., Roberts-Borsani et al. 2021b). Roman will detect galaxies up to $z \sim 15$ in case A and identify galaxies at $z \sim 13$ even in case B thanks to the wide survey areas. GREX-PLUS may be able to push the redshift frontier to $z \sim 17$ in case A. The wide-area surveys with Roman and GREX-PLUS can identify luminous $z > 10$ galaxies with $\lesssim 27$ mag. These galaxies are bright enough to be followed up by spectroscopically with ALMA and JWST within a reasonable amount of observing time, to investigate the physical conditions of these galaxies in the early universe.

7. Summary

In this paper we have presented our search for H -dropout LBGs at $z \sim 12$ –16. We have used the multiwavelength deep imaging data in the COSMOS and SXDS fields, including Subaru/HSC

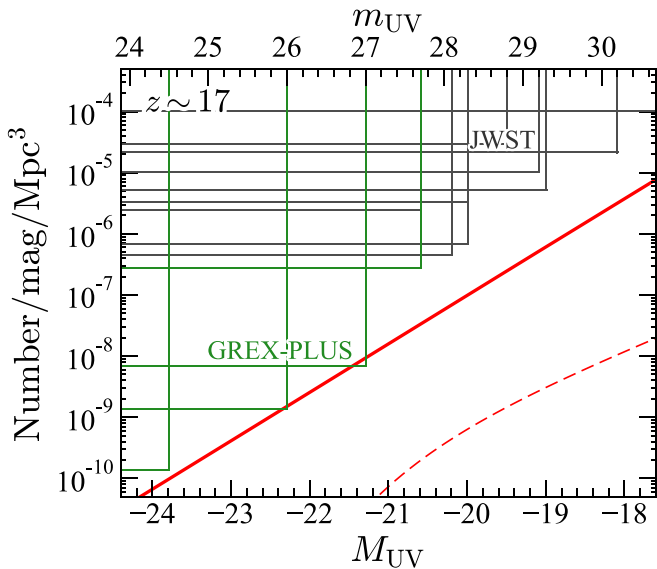


Figure 13. Same as Figure 11, but for $z \sim 17$. We only plot the survey depths and volumes of JWST and GREX-PLUS, which cover a wavelength redder than $2.3 \mu\text{m}$ (the Ly α break at $z \sim 17$).

grizy, VISTA *JHK_s*, UKIRT *JHK*, and Spitzer/IRAC [3.6][4.5] images. Our major findings are summarized below:

1. After the careful screening of foreground interlopers, we have identified two $z \sim 12$ – 13 galaxy candidates, HD1 and HD2 (Figure 2). SEDs of these candidates show a sharp discontinuity between *H* and *K_s* (*K*) bands, nondetections in the *grizyJ* bands, and a flat continuum up to the [4.5] band, all of which are consistent with a $z \sim 12$ – 13 galaxy. Photometric redshift analyses based on these SEDs indicate that the most likely redshifts are $z > 12$ for both HD1 and HD2.
2. We calculate the number density of our galaxy candidates whose mean redshift is $z \sim 13$ (Figure 7). The calculated number density at $z \sim 13$ is comparable to that of bright galaxies at $z \sim 10$ and consistent with the double-power-law luminosity function extrapolated to $z = 13$ assuming the redshift evolution in Bowler et al. (2020). These results support little evolution of the abundance of bright galaxies to $z \sim 13$ as suggested by previous studies at $z \sim 4$ – 10 . Comparisons with theoretical and empirical models show that these models underestimate the number densities of bright galaxies at $z \sim 10$ – 13 , although the uncertainties in observations are large (Figure 9). The inferred cosmic SFR density is consistent with the rapid decrease at $z > 10$ with $\propto 10^{-0.5(1+z)}$ suggested by Harikane et al. (2021b) (Figure 10).
3. We conducted ALMA follow-up observations targeting HD1. The obtained spectrum shows a $\sim 4\sigma$ tentative line-like feature at 237.8 GHz that is cospatial with the rest-frame UV emission, consistent with the O III 88 μm emission line at $z = 13.27$ (Figure 5). Further spectroscopic efforts are needed to confirm the redshifts of HD1 and HD2.

Our results support the possibility that a number of bright galaxies exist at $z > 10$. If the UV luminosity function follows the double-power-law function consistent with the number density of the bright galaxies at $z \sim 10$ – 13 , upcoming space

missions such as JWST, Roman, and GREX-PLUS will detect more than $\sim 10,000$ galaxies at $z \sim 13$ – 15 (Figures 11 and 12), and perhaps one to several at $z \sim 17$ (Figure 13), allowing us to observe the first galaxy formation.

We thank the anonymous referee for a careful reading and valuable comments that improved the clarity of the paper. We thank James Rhoads, Sangeeta Malhotra, Masami Ouchi, and the other members of the Roman cosmic dawn Science Investigation Team (SIT) for helpful discussions on the detectability of $z > 10$ galaxies with Roman. We are grateful to Caitlin Casey, James Dunlop, Steven Finkelstein, Christina Williams, and Rogier Windhorst for providing the expected depths in their JWST surveys, namely, COSMOS-Web, PRIMER, NGDEEP, PANORAMIC, and the Webb Medium-Deep Field survey, respectively. We thank Takashiro Morishita for bringing an error in Figure 6 in the earlier manuscript to our attention. This work was partly supported by the joint research program of the Institute for Cosmic Ray Research (ICRR), University of Tokyo, JSPS KAKENHI grant Nos. 17H06130, 19J01222, 20K22358, and 21K13953; the NAOJ ALMA Scientific Research Grant Codes 2018-09B and 2020-16B; and the black hole Initiative at Harvard University, which is funded by grants from the John Templeton Foundation and the Gordon and Betty Moore Foundation. T.H. was supported by Leading Initiative for Excellent Young Researchers, MEXT, Japan (HJH02007). P.D. and A.H. acknowledge support from the European Research Council’s starting grant ERC StG-717001 (“DELPHI”). P.D. also acknowledges support from the NWO grant 016.VIDI.189.162 (“ODIN”) and the European Commission’s and University of Groningen’s CO-FUND Rosalind Franklin program. A.Y. is supported by an appointment to the NASA Postdoctoral Program (NPP) at NASA Goddard Space Flight Center, administered by Oak Ridge Associated Universities under contract with NASA. F.P. acknowledges support from a Clay Fellowship administered by the Smithsonian Astrophysical Observatory.

This paper makes use of the following ALMA data: ADS/JAO. ALMA #2019.A.00015.S. ALMA is a partnership of ESO (representing its member states), NSF (USA) and NINS (Japan), together with NRC (Canada), MOST, and ASIAA (Taiwan), and KASI (Republic of Korea), in cooperation with the Republic of Chile. The Joint ALMA Observatory is operated by ESO, AUI/NRAO, and NAOJ.

This work is based on data products from observations made with ESO Telescopes at the La Silla Paranal Observatory under ESO program ID 179.A-2005 and on data products produced by CALET and the Cambridge Astronomy Survey Unit on behalf of the UltraVISTA consortium.

The HSC collaboration includes the astronomical communities of Japan and Taiwan, and Princeton University. The HSC instrumentation and software were developed by the National Astronomical Observatory of Japan (NAOJ), the Kavli Institute for the Physics and Mathematics of the Universe (Kavli IPMU), the University of Tokyo, the High Energy Accelerator Research Organization (KEK), the Academia Sinica Institute for Astronomy and Astrophysics in Taiwan (ASIAA), and Princeton University. Funding was contributed by the FIRST program from the Japanese Cabinet Office; the Ministry of Education, Culture, Sports, Science and Technology (MEXT); the Japan Society for the Promotion of Science (JSPS); Japan Science and Technology Agency (JST); the Toray Science

Foundation; NAOJ; Kavli IPMU; KEK; ASIAA; and Princeton University.






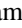








This paper makes use of software developed for the Large Synoptic Survey Telescope. We thank the LSST Project for making their code available as free software at <http://dm.lsst.org>

This paper is based on data collected at the Subaru Telescope and retrieved from the HSC data archive system, which is operated by Subaru Telescope and Astronomy Data Center (ADC) at NAOJ. Data analysis was in part carried out with the cooperation of the Center for Computational Astrophysics (CfCA), NAOJ.

The Pan-STARRS1 Surveys (PS1) and the PS1 public science archive have been made possible through contributions by the Institute for Astronomy, the University of Hawaii, the Pan-STARRS Project Office, the Max Planck Society and its participating institutes, the Max Planck Institute for Astronomy, Heidelberg, and the Max Planck Institute for Extraterrestrial Physics, Garching, Johns Hopkins University, Durham University, the University of Edinburgh, the Queens University Belfast, the Harvard-Smithsonian Center for Astrophysics, the Las Cumbres Observatory Global Telescope Network Incorporated, the National Central University of Taiwan, the Space Telescope Science Institute, the National Aeronautics and Space Administration under grant No. NNX08AR22G issued through the Planetary Science Division of the NASA Science Mission Directorate, the National Science Foundation grant No. AST-1238877, the University of Maryland, Eotvos Lorand University (ELTE), the Los Alamos National Laboratory, and the Gordon and Betty Moore Foundation.

Software: BEAGLE (Chevallard & Charlot 2016), PANHIT (Mawatari et al. 2020b), SExtractor (Bertin & Arnouts 1996), T-PHOT (Merlin et al. 2016).

ORCID iDs

Yuichi Harikane  <https://orcid.org/0000-0002-6047-430X>
 Akio K. Inoue  <https://orcid.org/0000-0002-7779-8677>
 Ken Mawatari  <https://orcid.org/0000-0003-4985-0201>
 Takuya Hashimoto  <https://orcid.org/0000-0002-0898-4038>
 Satoshi Yamanaka  <https://orcid.org/0000-0002-7738-5290>
 Yoshinobu Fudamoto  <https://orcid.org/0000-0001-7440-8832>
 Hiroshi Matsuo  <https://orcid.org/0000-0002-4559-6157>
 Yoichi Tamura  <https://orcid.org/0000-0003-4807-8117>
 Pratika Dayal  <https://orcid.org/0000-0001-8460-1564>
 L. Y. Aaron Yung  <https://orcid.org/0000-0003-3466-035X>
 Anne Hutter  <https://orcid.org/0000-0003-3760-461X>
 Fabio Pacucci  <https://orcid.org/0000-0001-9879-7780>
 Yuma Sugahara  <https://orcid.org/0000-0001-6958-7856>
 Anton M. Koekemoer  <https://orcid.org/0000-0002-6610-2048>

References

Adams, N. J., Bowler, R. A. A., Jarvis, M. J., et al. 2020, *MNRAS*, 494, 1771
 Aihara, H., AlSayyad, Y., Ando, M., et al. 2019, *PASJ*, 71, 114
 Aihara, H., Arimoto, N., Armstrong, R., et al. 2018, *PASJ*, 70, S4
 Ashby, M. L. N., Caputi, K. I., Cowley, W., et al. 2018, *ApJS*, 237, 39
 Bañados, E., Venemans, B. P., Mazzucchelli, C., et al. 2018, *Natur*, 553, 473
 Behroozi, P., Conroy, C., Wechsler, R. H., et al. 2020, *MNRAS*, 499, 5702
 Behroozi, P., Wechsler, R. H., Hearin, A. P., & Conroy, C. 2019, *MNRAS*, 488, 3143

Bertin, E., & Arnouts, S. 1996, *A&AS*, 117, 393
 Binggeli, C., Inoue, A. K., Hashimoto, T., et al. 2021, *A&A*, 646, A26
 Bouwens, R., González-López, J., Aravena, M., et al. 2020, *ApJ*, 902, 112
 Bouwens, R. J., Illingworth, G. D., Oesch, P. A., et al. 2015, *ApJ*, 803, 34
 Bouwens, R. J., Oesch, P. A., Labbé, I., et al. 2016, *ApJ*, 830, 67
 Bouwens, R. J., Oesch, P. A., Stefanon, M., et al. 2021, *AJ*, 162, 47
 Bowler, R. A. A., Jarvis, M. J., Dunlop, J. S., et al. 2020, *MNRAS*, 493, 2059
 Bruzual, G., & Charlot, S. 2003, *MNRAS*, 344, 1000
 Calzetti, D., Armus, L., Bohlin, R. C., et al. 2000, *ApJ*, 533, 682
 Carniani, S., Maiolino, R., Pallottini, A., et al. 2017, *A&A*, 605, A42
 Chabrier, G. 2003, *PASP*, 115, 763
 Chevallard, J., & Charlot, S. 2016, *MNRAS*, 462, 1415
 Coleman, G. D., Wu, C. C., & Weedman, D. W. 1980, *ApJS*, 43, 393
 da Cunha, E., Groves, B., Walter, F., et al. 2013, *ApJ*, 766, 13
 Davidzon, I., Ilbert, O., Laigle, C., et al. 2017, *A&A*, 605, A70
 Dayal, P., Dunlop, J. S., Maio, U., & Ciardi, B. 2013, *MNRAS*, 434, 1486
 Dayal, P., & Ferrara, A. 2018, *PhR*, 780, 1
 Dayal, P., Ferrara, A., Dunlop, J. S., & Pacucci, F. 2014, *MNRAS*, 445, 2545
 Dayal, P., Rossi, E. M., Shiralilou, B., et al. 2019, *MNRAS*, 486, 2336
 Dunlop, J. S., Abraham, R. G., Ashby, M. L. N., et al. 2021, JWST Proposal, Cycle 1, #1837
 Eisenstein, D. J., Ferruit, P., & Rieke, M. J. 2017a, JWST Proposal, Cycle 1, #1181
 Eisenstein, D. J., Ferruit, P., Rieke, M. J., Willmer, C. N. A., & Willott, C. J. 2017b, JWST Proposal, Cycle 1, #1180
 Ellis, R. S., McLure, R. J., Dunlop, J. S., et al. 2013, *ApJL*, 763, L7
 Finkelstein, S. L., Bagley, M., Song, M., et al. 2021a, arXiv:2106.13813
 Finkelstein, S. L., Dickinson, M., Ferguson, H. C., et al. 2017, JWST Proposal, Cycle 0, #1345
 Finkelstein, S. L., Papovich, C., Pirzkal, N., et al. 2021b, JWST Proposal, Cycle 1, #2079
 Finkelstein, S. L., Ryan, R. E., Jr., Papovich, C., et al. 2015, *ApJ*, 810, 71
 Fudamoto, Y., Oesch, P. A., Faisst, A., et al. 2020, *A&A*, 643, A4
 Furusawa, H., Kosugi, G., Akiyama, M., et al. 2008, *ApJS*, 176, 1
 Gehrels, N. 1986, *ApJ*, 303, 336
 Glazebrook, K., Schreiber, C., Labbé, I., et al. 2017, *Natur*, 544, 71
 Haiman, Z., & Menou, K. 2000, *ApJ*, 531, 42
 Harikane, Y., Fudamoto, Y., Hashimoto, T., et al. 2021, JWST Proposal, Cycle 1, #1740
 Harikane, Y., Ono, Y., Ouchi, M., et al. 2022, *ApJS*, 259, 20
 Harikane, Y., Ouchi, M., Inoue, A. K., et al. 2020, *ApJ*, 896, 93
 Harikane, Y., Ouchi, M., Ono, Y., et al. 2019, *ApJ*, 883, 142
 Harikane, Y., Ouchi, M., Shibuya, T., et al. 2018, *ApJ*, 859, 84
 Hashimoto, T., Inoue, A. K., Mawatari, K., et al. 2019, *PASJ*, 71, 71
 Hashimoto, T., Laporte, N., Mawatari, K., et al. 2018, *Natur*, 557, 392
 Hutter, A., Dayal, P., Yepes, G., et al. 2021, *MNRAS*, 503, 3698
 Inoue, A. K. 2011, *MNRAS*, 415, 2920
 Inoue, A. K., Shimizu, I., Iwata, I., & Tanaka, M. 2014a, *MNRAS*, 442, 1805
 Inoue, A. K., Shimizu, I., Tamura, Y., et al. 2014b, *ApJL*, 780, L18
 Inoue, A. K., Tamura, Y., Matsuo, H., et al. 2016, *Sci*, 352, 1559
 Jansen, R. A., & Windhorst, R. A. 2018, *PASP*, 130, 124001
 Jarvis, M. J., Bonfield, D. G., Bruce, V. A., et al. 2013, *MNRAS*, 428, 1281
 Jiang, L., Kashikawa, N., Wang, S., et al. 2021, *NatAs*, 5, 256
 Kartaltepe, J., Casey, C. M., Bagley, M., et al. 2021, JWST Proposal, Cycle 1, #1727
 Kirkpatrick, J. D., Cushing, M. C., Gelino, C. R., et al. 2011, *ApJS*, 197, 19
 Koekemoer, A., Foley, R. J., Spergel, D. N., et al. 2019, *BAAS*, 51, 550
 Labbe, I., Bezanson, R., Atek, H., et al. 2021, JWST Proposal, Cycle 1, #2561
 Laigle, C., McCracken, H. J., Ilbert, O., et al. 2016, *ApJS*, 224, 24
 Laporte, N., Ellis, R. S., Boone, F., et al. 2017, *ApJL*, 837, L21
 Laporte, N., Meyer, R. A., Ellis, R. S., et al. 2021, *MNRAS*, 505, 3336
 Lawrence, A., Warren, S. J., Almaini, O., et al. 2007, *MNRAS*, 379, 1599
 Madau, P., & Dickinson, M. 2014, *ARA&A*, 52, 415
 Marrone, D. P., Spilker, J. S., Hayward, C. C., et al. 2018, *Natur*, 553, 51
 Mason, C. A., Trenti, M., & Treu, T. 2015, *ApJ*, 813, 21
 Mawatari, K., Inoue, A. K., Hashimoto, T., et al. 2020a, *ApJ*, 889, 137
 Mawatari, K., Inoue, A. K., Yamanaka, S., Hashimoto, T., & Tamura, Y. 2020b, in Proc. IAU 341, Challenges in Panchromatic Modelling with Next Generation Facilities, ed. M. Boquien et al. (Cambridge: Cambridge Univ. Press), 285
 McCracken, H. J., Milvang-Jensen, B., Dunlop, J., et al. 2012, *A&A*, 544, A156
 McLeod, D. J., McLure, R. J., & Dunlop, J. S. 2016, *MNRAS*, 459, 3812
 McMullin, J. P., Waters, B., Schiebel, D., Young, W., & Golap, K. 2007, in ASP Conf. Ser., 376, Astronomical Data Analysis Software and Systems XVI, ed. R. A. Shaw, F. Hill, & D. J. Bell (San Francisco, CA: ASP), 127

- Mehta, V., Scarlata, C., Capak, P., et al. 2018, *ApJS*, **235**, 36
- Merlin, E., Bourne, N., Castellano, M., et al. 2016, *A&A*, **595**, A97
- Morishita, T., Trenti, M., Stiavelli, M., et al. 2018, *ApJ*, **867**, 150
- Mortlock, D. J., Warren, S. J., Venemans, B. P., et al. 2011, *Natur*, **474**, 616
- Oesch, P. A., Bouwens, R. J., Illingworth, G. D., Labbé, I., & Stefanon, M. 2018, *ApJ*, **855**, 105
- Oesch, P. A., Brammer, G., van Dokkum, P. G., et al. 2016, *ApJ*, **819**, 129
- Oke, J. B., & Gunn, J. E. 1983, *ApJ*, **266**, 713
- Oliver, S. J., Bock, J., Altieri, B., et al. 2012, *MNRAS*, **424**, 1614
- Ono, Y., Ouchi, M., Harikane, Y., et al. 2018, *PASJ*, **70**, S10
- Pacucci, F., Dayal, P., Harikane, Y., Inoue, A. K., & Loeb, A. 2022, arXiv:2201.00823
- Patten, B. M., Stauffer, J. R., Burrows, A., et al. 2006, *ApJ*, **651**, 502
- Piana, O., Dayal, P., & Choudhury, T. R. 2022, *MNRAS*, **510**, 5661
- Planck Collaboration, Ade, P. A. R., Aghanim, N., et al. 2016, *A&A*, **594**, A13
- Rhoads, J., Malhotra, S., Jansen, R. A., et al. 2018, AAS Meeting, **231**, 258.17
- Rieke, M. J., Kelly, D., & Horner, S. 2005, *Proc. SPIE*, **5904**, 1
- Roberts-Borsani, G., Morishita, T., Treu, T., Leethochawalit, N., & Trenti, M. 2021a, arXiv:2106.06544
- Roberts-Borsani, G., Treu, T., Mason, C., et al. 2021b, *ApJ*, **910**, 86
- Roberts-Borsani, G. W., Ellis, R. S., & Laporte, N. 2020, *MNRAS*, **497**, 3440
- Robertson, B. E. 2021, arXiv:2110.13160
- Rogers, A. B., McLure, R. J., Dunlop, J. S., et al. 2014, *MNRAS*, **440**, 3714
- Salpeter, E. E. 1955, *ApJ*, **121**, 161
- Sawicki, M. 2012, *PASP*, **124**, 1208
- Scoville, N., Aussel, H., Brusa, M., et al. 2007, *ApJS*, **172**, 1
- Shibuya, T., Miura, N., Iwadate, K., et al. 2022, *PASJ*, **74**, 73
- Speagle, J. S., Steinhardt, C. L., Capak, P. L., & Silverman, J. D. 2014, *ApJS*, **214**, 15
- Stark, D. P. 2016, *ARA&A*, **54**, 761
- Stefanon, M., Labbé, I., Bouwens, R. J., et al. 2017, *ApJ*, **851**, 43
- Stefanon, M., Labbé, I., Bouwens, R. J., et al. 2019, *ApJ*, **883**, 99
- Steidel, C. C., Adelberger, K. L., Giavalisco, M., Dickinson, M., & Pettini, M. 1999, *ApJ*, **519**, 1
- Stevans, M. L., Finkelstein, S. L., Wold, I., et al. 2018, *ApJ*, **863**, 63
- Tacchella, S., Bose, S., Conroy, C., Eisenstein, D. J., & Johnson, B. D. 2018, *ApJ*, **868**, 92
- Tacchella, S., Finkelstein, S. L., Bagley, M., et al. 2021, arXiv:2111.05351
- Tamura, Y., Mawatari, K., Hashimoto, T., et al. 2019, *ApJ*, **874**, 27
- Tanaka, M., Valentino, F., Toft, S., et al. 2019, *ApJL*, **885**, L34
- Treu, T. L., Abramson, L. E., Bradac, M., et al. 2017, JWST Proposal, Cycle 0, #1324
- Valentino, F., Tanaka, M., Davidzon, I., et al. 2020, *ApJ*, **889**, 93
- Walter, F., Riechers, D., Novak, M., et al. 2018, *ApJL*, **869**, L22
- Wang, F., Yang, J., Fan, X., et al. 2021, *ApJL*, **907**, L1
- Wang, T., Schreiber, C., Elbaz, D., et al. 2019, *Natur*, **572**, 211
- Weaver, J. R., Kauffmann, O. B., Ilbert, O., et al. 2022, *ApJS*, **258**, 11
- Williams, C. C., Oesch, P., Barrufet, L., et al. 2021, JWST Proposal, Cycle 1, #2514
- Willott, C. J., Albert, L., Arzoumanian, D., et al. 2010, *AJ*, **140**, 546
- Windhorst, R. A., Alpaslan, M., Ashcraft, T., et al. 2017, JWST Proposal, Cycle 1, #1176
- Yang, J., Wang, F., Fan, X., et al. 2020, *ApJL*, **897**, L14
- Yung, L. Y. A., Somerville, R. S., Finkelstein, S. L., Popping, G., & Davé, R. 2019, *MNRAS*, **483**, 2983
- Yung, L. Y. A., Somerville, R. S., Finkelstein, S. L., et al. 2020, *MNRAS*, **496**, 4574